

LONG-TERM X-RAY SPECTRAL VARIABILITY IN SEYFERT 1 GALAXIES

A. MARKOWITZ¹, R. EDELSON¹, S. VAUGHAN²

ABSTRACT

Direct time-resolved spectral fitting has been performed on continuous *RXTE* monitoring of seven Seyfert 1 galaxies in order to study their broadband spectral variability and Fe K_α variability characteristics on time scales of days to years. Variability in the Fe K_α line is not detected in some objects but is present in others, e.g., in NGC 3516, NGC 4151 and NGC 5548 there are systematic decreases in line flux by factors of $\sim 2\text{--}5$ over 3–4 years. The Fe K_α line varies less strongly than the broadband continuum, but, like the continuum, exhibits stronger variability towards longer time scales. Relatively less model-dependent broadband fractional variability amplitude (F_{var}) spectra also show weaker line variability compared to the continuum variability. Comparable systematic long-term decreases in the line and continuum are present in NGC 5548. Overall, however, there is no evidence for correlated variability between the line and continuum, severely challenging models in which the line tracks continuum variations modified only by a light-travel time delay. Local effects such as the formation of an ionized skin at the site of line emission may be relevant. The spectral fitting and F_{var} spectra both support spectral softening as continuum flux increases.

Subject headings: galaxies: active — galaxies: Seyfert — X-rays: galaxies

1. INTRODUCTION

There is substantial evidence to indicate that the central regions of Seyfert 1 Active Galactic Nuclei (AGN) consist of a geometrically-thin, optically-thick accretion disk surrounding a supermassive ($10^{6\text{--}9} M_{\odot}$) black hole. In the leading models, the inner disk is surrounded by a hot, optically-thin corona that Compton-upscatters soft photons thermally emitted from the disk to produce an X-ray power-law continuum over the range 1–100 keV, though the geometry of the corona remains uncertain (e.g., Haardt, Maraschi & Ghisellini 1994). Furthermore, some optically thick material, such as the accretion disk, intercepts and reprocesses some of the X-rays, producing the so-called Compton reflection hump above ~ 10 keV and a strong Fe K_α fluorescent emission line at 6.4 keV (Guilbert & Rees 1988, George & Fabian 1991). Though the exact configuration of accreting material throughout the central engine is not known, the Fe K_α line, as a primary signature of the reprocessing, serves as a potential tool to trace the distribution of accreting gas.

Single-epoch spectral fitting has revealed a variety of profiles for the Fe K_α line. In some Seyfert 1 galaxies, the line is seen to be relativistically broadened (e.g., FWZI up to 100,000 km s⁻¹ in the well-studied broad line profile of MCG-6-30-15, Tanaka et al. 1995) and redshifted. This can be explained in terms of a line originating in the innermost regions of the accretion disk, in close proximity to the black hole, and affected by strong Doppler and gravitational redshifts (Fabian et al. 1995). However, the majority of Seyfert 1 galaxies observed with *XMM-Newton* (Reeves 2002) and *Chandra* (Yaqoob, George & Turner 2001) feature a narrow Fe K_α component, modelled to be only mildly broadened, with FWHMs of $< 10,000$ km s⁻¹ (e.g., Kaspi et al. 2002, Nandra 2001, O’Brien et al. 2001, Yaqoob et al. 2001). For these objects, a line origin in

the outer accretion disk, putative molecular torus, broad emission line region or narrow emission line region may be more relevant.

Studying the time-resolved variability of the line and continuum components provides a complementary analysis to single-epoch spectral fitting. For instance, Fe K_α line emission originating in close proximity to the central black hole is expected to respond rapidly to changes in the illuminating continuum flux (Stella 1990, Matt & Perola 1992). The simplest models predict that if the reprocessing time scale is negligible, then variations in the Fe K_α line should track continuum variations, modified only by a time delay equal to the light-crossing time across the inner disk. However, recent studies have not been able to support this picture. Investigations into the behavior of the broad Fe K_α line in MCG-6-30-15 by Iwasawa et al. (1996, 1999), Lee et al. (1999), Reynolds (2000), Vaughan & Edelson (2001, hereafter VE01), and Fabian et al. (2002) have confirmed the presence of rapid Fe K_α line variability in this object, but have found the line to vary considerably less strongly than the continuum, and have found no correlation between continuum and line variations. Yaqoob et al. (1996) found the red wing of the Fe K_α profile in NGC 7314 to respond to rapid continuum variations, while the core did not respond as rapidly. Conversely, Nandra et al. (1999) found that the narrow core of the line in NGC 3516 tracked the continuum flux, while the broad wings displayed uncorrelated variability. Petrucci et al. (2002) used *XMM-Newton* to obtain two observations of Mkn 841 separated by 15 hours; while the continuum flux and shape stayed nearly constant between the two observations, the narrow line virtually disappeared.

This paper aims to study the broadband spectral variability of Seyfert 1 galaxies on time scales of days to years. This includes quantifying the variability of the Fe K_α line and determining the relation between the line and the con-

¹ Dept. of Astronomy, Univ. of California, Los Angeles CA 90095-1562; agm@astro.ucla.edu, rae@astro.ucla.edu

² Institute of Astronomy, Madingley Road, Cambridge, CB3 0HA, UK; sav@ast.cam.ac.uk

tinuum flux. To this end, samples have been assembled that probe spectral variability on time scales of days to weeks (hereafter referred to as “short” time scales) and time scales of months to years (hereafter referred to as “long” time scales), using archival monitoring data from the *Rossi X-ray Timing Explorer (RXTE)*. *RXTE* provides the largest effective area at 6 keV of any current X-ray instrument flown to date and thus offers the highest signal-to-noise of the Fe K region of the X-ray spectrum. The data reduction and sampling are described in §2. In order to track the line behavior, direct time-resolved spectral fitting has been systematically performed and fractional variability amplitude spectra have been constructed, presented in §3. The observational results are summarized in §4. The physical implications are discussed in §5, followed by a brief summary of the main results in §6.

2. DATA COLLECTION AND REDUCTION

The goal of this project was to obtain uniform samples to survey line and continuum variability behavior. Continuous *RXTE* archival monitoring data turning public before 2002 December, when these analyses were performed, were used, as well as the authors’ proprietary observations of three Seyfert 1 galaxies observed during Cycle 7.

All *RXTE* data considered in this paper were obtained with the proportional counter array (PCA). 3–18 keV count rates were estimated with the online W3PIMMS tool, using mean 2–10 keV archival count rates and photon indices obtained either from previously published fits (e.g., Kaspi et al. 2001) or the Tartarus database. The goal of time-resolved spectral fitting was to obtain at least ten high-quality spectra with at least $\sim 50,000$ photons in each time bin; sources that failed to meet this criterion were excluded. This resulted in eight observations consisting of continuous monitoring on short time scales (e.g., sources observed once every 1–2 orbits for ~ 1 ks over a span of ~ 30 days) and an additional seven observations covering long time scales (e.g., sources observed once every 3 or 4 days for several years). There were six objects common to both lists. This included two MCG–6–30–15 observations on short time scales, an 8-day intensive scan henceforth denoted as short-term MCG–6–30–15 (I) and a 53-day observation denoted as short-term MCG–6–30–15 (II). This also included two MCG–6–30–15 observations on long time scales, one spanning 326 days denoted as long-term MCG–6–30–15 (I) and a 2093-day observation denoted as long-term MCG–6–30–15 (II). Additionally, NGC 7469 was monitored only on the short time scale. Table 1 lists the date ranges and source parameter information.

The PCA consists of five identical collimated proportional counter units (PCUs; Swank 1998). For simplicity, data were collected only from those PCUs that did not suffer from repeated breakdown during on-source time (PCUs 0, 1, and 2 prior to 1998 December 23; PCUs 0 and 2 from 1998 December 23 until 2000 May 12; PCU 2 only after 2000 May 12). Count rates quoted in this paper are normalized to 1 PCU. Only PCA STANDARD-2 data were considered. The data were reduced using standard extraction methods and FTOOLS v5.2 software. Data were rejected if they were gathered less than 10° from the Earth’s limb, if they were obtained within 30 min after the satel-

lite’s passage through the SAA, if ELECTRON0 > 0.1 (ELECTRON2 after 2000 May 12), or if the satellite’s pointing offset was greater than $0^\circ 02$.

As the PCA has no simultaneous background monitoring capability, background data were estimated by using PCABACKEST v2.1E to generate model files based on the particle-induced background, SAA activity, and the diffuse X-ray background. This background subtraction is the dominant source of systematic uncertainty (e.g., in total broadband count rate) in *RXTE* AGN monitoring data (e.g., Edelson & Nandra 1999). Counts were extracted only from the topmost PCU layer to maximize the signal-to-noise ratio. All of the targets were faint ($< 40 \text{ ct s}^{-1} \text{ PCU}^{-1}$), so the most recent versions of the ‘L7-240’ background models were used. Source and background spectra were derived over the time intervals listed in Table 1. These time bins were chosen to ensure adequate signal-to-noise in the Fe K_α line in the time-resolved fits, but also to ensure adequate temporal resolution in determining the variability characteristics of both the continuum and the line. Response matrices were generated for each gain epoch using PCARSP v.8.0.

3. ANALYSIS

The time-averaged fits, described in §3.1, were performed with the goal of minimizing the number of free parameters needed to produce an acceptable fit. These model fits were then applied to the time-resolved data, as described in §3.2. The errors on parameters derived from spectral fitting are discussed in §3.3. The time-resolved spectral fitting is discussed in §3.4. Continuum and line variability amplitudes are presented in §3.5. Temporal cross-correlation analysis is described in §3.6. Finally, the fractional variability amplitude (F_{var}) spectra are described in §3.7.

3.1. Time-Averaged Spectral Fitting

For all analyses, data below 3.5 keV were discarded in order to disregard PCA calibration uncertainties below this energy and also to reduce the effects of warm absorbers in sources (e.g., MCG–6–30–15, Reynolds 1997; NGC 3783, Kaspi et al. 2002; NGC 5548, Nicastro et al. 2000). Data above 18 keV were discarded as the source count rate became too low at higher energies to obtain a good detection in each time bin. All spectral fitting was done with XSPEC v.11.0.2 (Arnaud 1996). Most long-term observations spanned multiple gain epochs, requiring simultaneous fitting of data sets.

For all observations, the simple model of a power-law modified by cold absorption resulted in large residuals near 6 keV due to the Fe K_α line; the addition of a emission component proved significant at greater than 99.99% confidence in an F-test. Given the limit of PCA calibration (data/model residuals $\lesssim 2\text{--}3\%$ ¹, and the low energy resolution of the PCA (~ 1 keV at 6 keV), the PCA is largely insensitive to the detailed shape of the Fe K_α line. Both a single Gaussian and a Laor model component (diskline model for a maximally rotating Kerr black hole; Laor 1991) were tested to parameterize the line emission. More complex fits such as double Gaussians or a Laor component

¹ See <http://lheawww.gsfc.nasa.gov/users/keith/rossi2000/energy-response.ps>

plus a narrow Gaussian were either not required or did not yield sensible results; the single-Gaussian and Laor fits alone gave sensible results. For the Laor model component, the inclination angle was kept fixed at 30°, and the outer radius kept fixed at 400 gravitational radii; in no case did thawing either or both of these parameters measurably improve the fits. The emissivity index β was constrained to fall in the range 0.0–9.9. Laor models gave significantly better fits (at >99% confidence in an F-test) than the single-Gaussian parameterization in seven of the fifteen time-averaged spectra. An implicit assumption in these fits is that the emission regions in each source do not evolve substantially (i.e., major changes in the geometry of the emitting regions) throughout the duration of the observation.

For all sources except NGC 4151, neutral absorption was kept fixed at the Galactic value. For NGC 4151, modelling the column density with a value much higher than Galactic resulted in a significant (>99.99% confidence in an F-test) improvement in the model fit. The column density values obtained, given the PCA calibration, were in reasonable agreement with each other and with the value of $4.6 \pm 0.2 \times 10^{22} \text{ cm}^{-1}$ in the spectral fit by Schurch & Warwick (2002).

For all model fits except the short time scale observation of 3C 390.3 and the Laor model fit to the short time scale observation of NGC 3516, there were residuals above 10 keV that signalled the need to incorporate a Compton reflection hump. Including a PEXRAV component to model reflection of an underlying power law component off optically thick and neutral material (Magdziarz & Zdziarski 1995) provided the necessary improvement to the fits, significant at greater than 99% confidence compared to models with just a power-law plus Fe K_α line, modified by cold absorption. In the PEXRAV component, the inclination angle of the reflector was kept fixed at 30°, and the power-law cutoff energy was kept fixed at 100 keV. All element abundances were kept fixed at solar; as noted by VE01 a change in Fe abundance caused the absolute values of spectral fit parameters to change slightly, but the variability pattern, the focus of this paper, remained unchanged.

The basic model thus used, a power-law component plus PEXRAV (where applicable) plus a parameterization for the Fe K_α line as described above, all modified by neutral absorption, gave reasonable fits to the data. The exceptional signal-to-noise in these time-averaged spectra invariably meant that systematic errors associated with the background modelling and spectral response of the PCA dominated the uncertainties. Consequently, finding a statistically acceptable time-averaged fit (with $\chi^2_\nu \sim 1$) was unlikely even if the model was representative of the intrinsic spectrum of the source. The data/model residuals seen were consistent with the limit of the PCA calibration. Tables 2–3 summarize the time-averaged fitting results for both the single-Gaussian and Laor models, respectively, on both time scales.

While higher-resolution X-ray instruments can detect one or both of the Fe K_α broad and narrow components, the PCA is sensitive only to the combined flux of the two components. Recent *XMM-Newton* model fits can provide insight as to which component, the broad or narrow, dominates the *RXTE* view in each object. (*Chandra*-HETG

can additionally constrain the narrow component but is mostly insensitive to the broad component.) For instance, the equivalent width of the broad component has been measured to be much greater than that of the narrow component in both MCG–6–30–15 (Wilms et al. 2001) and NGC 3516 (Turner et al. 2002). The present *RXTE* fits also indicated that the Fe K_α lines in these two objects are among the broadest of the sample, consistent with the bulk of the line emission originating in the inner accretion disk. In contrast, the narrow component seems to dominate in NGC 4151 (Schurch et al. 2002), NGC 5548 (Pounds et al. 2003, Yaqoob et al. 2001) and NGC 7469 (Blustin et al. 2003), with a small upper limit or no detection of the broad component. The present *RXTE* fits for NGC 4151, for instance, indicated the narrowest line of the sample, consistent with emission far from the central black hole. The equivalent widths of the broad and narrow components in NGC 3783 are approximately equal (Blustin et al. 2002), indicating that emission from both the inner accretion disk and a more distant location is relevant in this source.

3.2. Time-Resolved Spectral Fit Components

The above models were then applied to the time-resolved data. Spectral fits to time bins spanning gain epoch changes required simultaneous fitting of the two data sets. The Fe K_α line was always detected in each time bin, as the addition of a line emission component was significant at >99% confidence in an F-test for nearly every time bin (in the single exception, the last time bin of the long time scale observation of NGC 5548, it was significant only at 98.1% confidence). While fitting the time-averaged models to their respective time-resolved spectra, it was not practical to thaw parameters such as the Fe K_α line profile shape (line width in the single-Gaussian models; inner radius and emissivity index β in the Laor models) or line peak energy, given the PCA resolution and sensitivity. The F-test was used to determine which free parameters to include in the fit. The time-resolved spectral fits were repeated with each of photon index Γ , reflection fraction R (ratio of the reflection normalization at 1 keV to the normalization of the power law) and line flux normalization $F_{K\alpha}$ frozen at their time-averaged values, and the values of total χ^2 were compared via an F-test to determine which parameters could justifiably be allowed to be free and which should be kept fixed in the fitting, as listed in Table 4. There was no formal significant evidence (>99.7% confidence) of the need to thaw R in any object. For most sources (6/8 short time scale and 6/7 long time scale observations), there was significant (>99.7% confidence) evidence of the need to thaw Γ . There was also significant (>99.7% confidence) evidence of the need to thaw $F_{K\alpha}$ in the short time scale observations of MCG–6–30–15 (I), NGC 3516 and NGC 7469 as well as in the long time scale observations of MCG–6–30–15 (II), NGC 3516 and NGC 4151. These results initially suggest statistically significant variations in the line in at least some of these objects. Table 5 lists the mean values of the 2–10 keV flux $F_{2–10}$, Γ and $F_{K\alpha}$ derived from the time-resolved spectral fitting. $F_{2–10}$ was measured from the model fits.

3.3. Error Estimation

For the majority of the individual time-resolved fits, the resulting values of the fit statistic χ^2_ν were rather low ($\chi^2_\nu < 1.0$ for 243 of the 316 total time bins). As discussed by Nandra et al. (2000) and VE01, this was most likely due to the standard software's overestimation of the errors in any given energy bin in the net spectrum. These errors are produced by combining the errors in the source with those of the modelled background. The software uses Poisson statistics, estimated from a large quantity of background data, to estimate the background error. For short exposures, this results in an overestimate of background errors, which should typically be negligible compared to the error on the total (source plus background) rate. To better ascertain the variability of the measured spectral parameters, the standard errors produced by the software were discarded and new 1σ errors were estimated based on the variability properties of the derived light curves. The point-to-point variance was used; this is defined as

$$\sigma_{PP}^2 = \frac{1}{2} \frac{1}{N-1} \sum_{i=1}^{N-1} (x_i - x_{i+1})^2$$

where x_i are each of the N total points in the light curve. VE01 used simulations to validate the accuracy of these errors. These are conservative error estimates; only trends in the light curves sustained over several time bins will exceed the expected error using this formulation. These errors are listed in Table 5 for Γ and $F_{K\alpha}$ and used hereafter. Errors on values of F_{2-10} within a time bin were determined from the 2–10 keV continuum light curve, using the mean flux error on the ~ 1 ks exposures in that time bin.

3.4. Time-Resolved Broadband Spectral Fits

Figures 1 and 2 show light curves of F_{2-10} , Γ , and $F_{K\alpha}$ for the single-Gaussian model on short and long time scales, respectively. The results of the Laor model time-resolved fits showed identical variability patterns and nearly identical time-averaged values to the single-Gaussian fits, and they are not plotted.

This spectral fitting was performed keeping the value of R fixed, i.e. with the normalization of the PEXRAV reflection component varying in sync with the normalization of the power-law. This was done as there was no formal statistical requirement to allow the value of R to vary in the fits; freezing R also minimized the influence of this free parameter on measurement of Γ and $F_{K\alpha}$. However, as the reflection continuum and Fe $K\alpha$ line are likely to be produced in the same location (e.g., the accretion disk) it would perhaps be expected that the reflection component tracks variations in the line rather than the power-law continuum. Time-resolved spectral fitting was repeated with the normalization of the reflector tied to the $F_{K\alpha}$ instead. The resulting light curves of $F_{K\alpha}$ were essentially the same as those with a fixed value of R .

3.5. Fractional Variability Amplitudes

Fractional variability amplitudes (F_{var} ; e.g., Vaughan et al. 2003, Edelson et al. 2002) were measured to quantify the intrinsic variability amplitude relative to the mean count rate and in excess of the measurement noise in the

continuum and line light curves;

$$F_{var} = \sqrt{\frac{S^2 - \langle \sigma_{err}^2 \rangle}{\langle X \rangle^2}}, \quad (1)$$

where S^2 is the total variance of the light curve, $\langle \sigma_{err}^2 \rangle$ is the mean square error and $\langle X \rangle$ is the mean count rate of N total points. The error on F_{var} is

$$\sigma_{F_{var}} = \sqrt{\left\{ \sqrt{\frac{\langle \sigma_{err}^2 \rangle}{N}} \cdot \frac{1}{\langle X \rangle} \right\}^2 + \left\{ \sqrt{\frac{1}{2N}} \cdot \frac{\langle \sigma_{err}^2 \rangle}{\langle X \rangle^2 F_{var}} \right\}^2} \quad (2)$$

as discussed in Vaughan et al. (2003). This error formulation estimates $\sigma_{F_{var}}$ based on random errors in the data itself, and not due to random variations associated with red-noise processes. Furthermore, these estimates are only an approximation to the true values of $\sigma_{F_{var}}$ since the data errors used here instead have been estimated from the point-to-point variance. Table 6 lists the continuum and line variability amplitudes.

3.6. Cross Correlation Analysis

Temporal cross-correlation functions were calculated for F_{2-10} – $F_{K\alpha}$, F_{2-10} – Γ , and Γ – $F_{K\alpha}$ using both the discrete correlation Function DCF (Edelson & Krolik 1988) and the interpolated correlation function (ICF, White & Peterson 1994). ICF lag uncertainties were calculated using the bootstrap method of Peterson et al. (1998); however, this method often underestimates the true errors introduced by uneven sampling, e.g., Edelson et al. (2001). Figures 3 and 4 and Tables 7–9 show the cross-correlation results, where a positive shift denotes the first quantity leading the second. The DCF and ICF time bins used were 1.0 and 0.5 times the time bin size in the time-resolved fits, respectively.

One must be skeptical of cross-correlation analysis in these circumstances, however, due to the red-noise nature of the continuum and line fluxes (as speculated below). Cross-correlation between two unrelated red-noise noise light curves can randomly yield spurious correlations with higher than expected values of the correlation strength r_{max} (e.g., Welsh 1999). For instance, the $r_{max} = 0.7$ optical-to-X-ray lag in NGC 3516 claimed by Maoz et al. (2000) was not confirmed with additional data by Maoz et al. (2002). Combined with the fact that most of these light curves only have 10–20 points, spurious correlations and anticorrelations, including those based on very few points (i.e., trends much shorter than the total duration), can arise. Discarding peak lags greater than $\sim 1/3$ of the total duration can eliminate some of these spurious lags; this has been done for the values reported in Tables 7–9 and the functions plotted in Figures 3 and 4. However, as has been done in the present work, it is more practical to not trust any lag where r_{max} is not very close to 1.0, applying relatively more skepticism for lower values of r_{max} .

Cross-correlation analysis of F_{2-10} and $F_{K\alpha}$ in the short time scale observations yields peak correlation coefficients in the range 0.17–0.72. These values do not readily convince us that the analysis has yielded 'believable' correlations. For instance, the highest correlation coefficient, $r_{max} = 0.72$, arises in NGC 3783, which only has 12 points and for which substantial variability in the line is

not detected (see Table 4). NGC 5548, for which cross-correlation analysis yields the second-highest value of r_{max} in the short time scale sample, is a similar situation: the reported lag is far from zero, based on only a handful of points, and one cannot conclude that this is a reliable correlation robustly detected in excess of the long time scale red-noise variations present. It follows that the lag delays and lag errors listed in Table 7 must also be regarded with a large dose of skepticism.

For long time scale F_{2-10} – $F_{K\alpha}$ correlations, the values of r_{max} lie in the range 0.45–0.87. Despite the presence of higher values of r_{max} , however, caution is again warranted. For instance, as the continuum and line light curves are both dominated by large decreases in NGC 3516 and NGC 5548, the resulting cross-correlation functions have moderately-high values of the correlation coefficient at nearly all lags tested, and the peak correlation coefficients do not provide evidence of a strong correlation “in excess” of this artefact. If there were an increase in the values of r_{max} towards a particular time scale, this would indicate more of a physical relevance associated with that time scale. However, only three objects show an increase in their respective values of average DCF and ICF r_{max} towards longer time scales.

Γ – $F_{K\alpha}$ cross-correlation functions show similar correlation coefficient values as the F_{2-10} – $F_{K\alpha}$ cross-correlation functions. However, many cross-correlation functions between F_{2-10} and Γ on both time scales yield higher values of r_{max} . The values of r_{max} on short time scales span 0.54–0.92; those on long time scales span 0.31–0.94 (0.62–0.94 if NGC 4151 is excluded). All but one of the lag delays are consistent with zero.

3.7. F_{var} Spectra

F_{var} spectra, measuring F_{var} of the net (background-subtracted) count rate in each channel, were calculated as a relatively less model-dependent assessment of the broadband spectral variability. Such analysis allows one to study the behavior of the varying components. Source and background spectra were derived over the time intervals listed in Table 10 with the goal of constructing light curves of the flux in each channel for at least ~ 20 points. In addition to the observations used in the above analysis, F_{var} spectra were measured for an additional four objects on short time scales and five objects on long time scales; the total of twelve observations on each time scale included nine objects common to both lists. Because the PCU gain settings changed three times since launch and the channel energy boundaries differ between gain epochs, the longest duration that did not cross a gain epoch boundary was used. The error on each light curve point was assigned using the point-to-point variance (see §3.3). The highest-energy bins were re-grouped as necessary to insure adequate signal-to-noise in all energy bins. For the soft-spectrum ($\Gamma \sim 2.7$; Vaughan et al. 1999) source Akn 564, data above 9 keV were discarded to minimize the influence of systematic variability in the *RXTE* background models. Similarly, in Fairall 9 ($\Gamma \sim 2.2$ over 2–10 keV, TARTARUS database), data above 14.3 keV were discarded for the short time scale data. F_{var} and $\sigma_{F_{var}}$ were calculated in each channel using the equations in §3.5. The final F_{var} spectra are presented in Figures 5 and 6 for short and long time

scales respectively. For the seven sources with published power spectral densities (Markowitz et al. 2003, Uttley, McHardy & Papadakis 2002), the relative continuum variability amplitudes obtained on short and long time scales are in reasonable agreement with values predicted from their published power spectral density shapes.

4. RESULTS

A summary of the observed continuum broadband flux and spectral variability properties of the sample is given in §4.1. The observed line variability properties are summarized in §4.2. Finally, a comparison between the continuum and line variability properties is given in §4.3. Notes on individual sources are deferred to Appendix A.

4.1. Continuum variability

All objects display significant variability in continuum flux: in χ^2 -tests against the constant hypothesis, the constant hypothesis is rejected at $>99.99\%$ confidence for all continuum light curves. Visual inspection of Figures 1 and 2 confirms this. There is evidence for the continuum to vary more strongly towards longer time scales: of the six objects with both short- and long time scale monitoring, the value of continuum F_{var} increases towards longer time scales for five objects. The F_{var} spectra also exhibit stronger continuum variability on longer time scales in most sources. Both these analyses support an increase in variability amplitude towards longer time scales that is consistent with the long-established red-noise nature of Seyfert 1 continuum X-ray emission.

The majority of F_{var} spectra show the softer energies to be the most variable, consistent with softening of the dominating broadband X-ray continuum as sources brighten (e.g., Markowitz & Edelson 2001, Nandra et al. 1997). The only exception is Akn 564, which exhibits a much flatter dependence on F_{var} with energy. The presence of F_{2-10} – Γ correlations with no measurable lags in many objects on both time scales supports this idea. Such behavior has been observed numerous times before (e.g., VE01, Done et al. 2000, Lee et al. 2000, Chiang et al. 1999, Nandra, Pounds & Stewart 1990).

Above ~ 10 keV, unmodelled systematic variations in the background can contribute greatly to the total observed variability. In most sources, therefore, the influence of the variability of the Compton reflection hump on the broadband continuum above ~ 10 keV cannot be reliably constrained from the F_{var} spectra.

4.2. $Fe\ K\alpha$ line variability

Given that the 5–7 keV continuum flux greatly outshines the line flux and given the nature of spectral fitting, it is possible that there could exist some systematic effect that corrupts the determination of the continuum level at the \sim few per cent level, in turn corrupting determination of the line flux by ~ 10 percent or higher. However, such an effect is not readily identifiable, and the line variations measured are hence assumed intrinsic to the sources.

Time-resolved spectral fitting has revealed a wide range of variability in the line on both time scales. On short time scales, MCG–6–30–15 (I) shows evidence for line variability: a χ^2 -test against a constant hypothesis results in rejection of that hypothesis at $>99\%$ confidence. Similarly,

the constant hypothesis is rejected in MCG-6-30-15 (II) and NGC 3516, but only at 98% and 95% confidence, respectively.

On long time scales, the number of objects showing line variability increases: in three of the seven observations (NGC 3516, NGC 4151 and NGC 5548), the constant line flux hypothesis is rejected at $>99.99\%$ confidence. In two additional observations, MCG-6-30-15 (I) and 3C 390.3, the constant line flux hypothesis is rejected, but only at 97.9% and 97.7% confidence, respectively. The most notable trends in line flux are the gradual decreasing trends throughout the long time scale observations of NGC 3516, NGC 4151 and NGC 5548. Lack of line variability cannot be ruled out in MCG-6-30-15 (II) and NGC 3783. Overall, one can conclude that Fe K_{α} line variability is more commonly detected towards longer time scales.

This tendency is confirmed using measured values of F_{var} : the value of line F_{var} increases towards longer time scales for four objects, the values of line F_{var} on both time scales are consistent for the remaining two objects, and in no case does line F_{var} decrease towards longer time scales. It is therefore plausible to conclude that, at least on the time scales probed herein, the iron line variability is, like the continuum variability, a red-noise process.

The average maximum peak-to-trough line flux variation detected is a factor of ~ 2 for all observations; typically, this is a factor of ~ 4.5 greater than the typical error bar. The largest peak-to-trough variations are ~ 3 , as in the short-term observation MCG-6-30-15 (II) and the long-term observations of NGC 4151 and NGC 5548. The smallest peak-to-trough variations are $\sim 40\text{--}50\%$, as with the short-term observations of NGC 3516 and NGC 3783 and the long-term observations MCG-6-30-15 (II) and NGC 3783; typically this is a factor of ~ 2 greater than the typical error bar. With the time bins chosen in this experiment to maximize the variability-to-noise in the iron line light curves, this experiment may not be sensitive to smaller amplitudes of variability (peak-to-trough variations of $\sim 30\%$ or less).

4.3. Relating continuum and line variability

Visual examination of the continuum and line light curves does not reveal any obvious relation between them in most objects. Large-amplitude trends in continuum often go unmatched by simultaneous changes in the line; prominent examples of this are listed for individual sources below. In only a few observations do the continuum and line appear to track each other: in the long time scale observation of NGC 5548, both the continuum and line decrease by a factor of ~ 3 over the 4-year duration. There are also somewhat similar decreasing trends dominating both the continuum and line in the long-time scale observations of NGC 3516 and NGC 4151.

Measured variability amplitudes, F_{var} spectra, and the increased detection of line variability in the light curves towards longer time scales all indicate that both the continuum and line appear to be more strongly variable towards longer time scales in most objects. However, there is evidence that the line does not vary as strongly as the continuum. In 11/15 observations, the value of continuum F_{var} is greater than the line F_{var} . For the eight of these eleven observations with a defined value of line F_{var} (positive ex-

cess variance), the continuum and line excess variances are compared via an F-test. In six of these eight observations, the null hypothesis of the continuum and line excess variances being consistent is rejected at $>98.2\%$ confidence. In four of the fifteen observations, the values of continuum and line F_{var} are consistent with each other. For three of these observations, an F-test cannot reject the null hypothesis of the continuum and line excess variances being consistent at greater than 79% confidence; it is rejected at $>99.99\%$ confidence in the fourth observation (the long-term NGC 3783 observation). There are no observations with a larger value of F_{var} for the line compared to the continuum.

As seen in Figures 5 & 6, in many of the F_{var} spectra, there is a reduction in variability at ~ 6 keV. The average drop in F_{var} at ~ 6 keV relative to the surrounding continuum is $\sim 10\%$, or ~ 5 times larger than the typical errors. Best fit lines to the F_{var} spectra including and excluding the $\sim 5\text{--}7$ keV region indicate that the dip is significant at greater than 90% confidence in an F-test for 11/24 observations. These dips are consistent with dilution of the $\sim 5\text{--}7$ keV continuum variability by relatively reduced line variability. Such a feature has been noted previously in the F_{var} spectra of NGC 4151 (Schurch & Warwick 2002) and MCG-6-30-15 (Fabian et al. 2002). The presence of this feature supports the argument for decoupling of the line and continuum variability properties. Additionally, cross-correlation analysis does not reveal any significant temporal correlations between continuum and line variations.

Overall, there hence is little support for a simple or direct temporal relation between the observed continuum and Fe K_{α} line variability properties. This result broadly agrees with the study of Weaver, Gelbord & Yaqoob (2001), who did not find any evidence that Fe K_{α} line variability on time scales of days to years was correlated with continuum variations; their *ASCA* sample included all of the objects in this paper's time-resolved spectroscopy samples except 3C 390.3, though with much less continuous sampling.

5. DISCUSSION

This paper examines the variability properties of both the continuum and Fe K_{α} line on time scales from days to years. The continuum variability properties observed in the current sample have been observed before in many Seyfert 1 galaxies. The data show an increase in broadband variability amplitude towards longer time scales, demonstrating the red-noise nature of the continuum variability. Additionally, there is an increase in variability amplitude towards the softer X-rays, consistent with sources' softening as they brighten. In contrast, the Fe K_{α} line shows a divergence of behaviors. Most observations show no clear trend whatsoever. Only a few observations show temporal trends in the line flux that mimic the continuum to at least some degree, and only on time scales of years. As discussed in §4.3, however, the line varies less strongly than the continuum in many sources, as seen from a comparison of the spectral fit line and continuum flux light curve variability amplitudes as well as from a reduction in broadband F_{var} near 6 keV seen in many sources' F_{var} spectra. The relationship between continuum and

line variability is examined further in §5.1. The broadband spectral variability results are discussed in §5.2.

5.1. $Fe\ K_{\alpha}$ line variability

This paper has demonstrated the presence of a range of variability behavior in the $Fe\ K_{\alpha}$ line. The results permit tests of simple models in which the bulk of the continuum originates in a central corona and the line variations are driven solely by continuum flux fluctuations modified by light-travel time effects. For instance, such models imply that there should exist a connection between the origin of the line emission (which can be inferred from the resolved profile shape) and the presence of rapid line variability. If the bulk of the line is emitted in the inner accretion disk (as implied by the broad line profiles in MCG-6-30-15 and NGC 3516), then the continuum and line variations should be correlated on time scales comparable to the light crossing time of the inner accretion disk. This is because the reprocessing times are likely very short compared to the light travel times, which dominate the correlation. However, the time bins used in this paper are typically at least two orders of magnitude longer than the expected light crossing time scale of the putative inner accretion disk. This means that any variations on this time scale would be grossly undersampled.

If the bulk of the line is emitted far from the central corona (e.g., as implied by the narrow line profiles for NGC 4151 and NGC 5548), then one would expect the line variations to track the continuum variations only on sufficiently long time scales (e.g., longer than days–weeks if the line is emitted in a region coincident with the broad line region; Kaspi et al. 2000). For instance, the presence of similar long-term trends in the continuum and line in NGC 5548 supports a model in which the bulk of the line emission originates far from the central corona in this object. More specifically, it is consistent with the prediction of Yaqoob et al. (2001) that the flux of the narrow core in NGC 5548, estimated to originate in a region consistent with the broad line region in this object, should track the continuum flux on time scales of $\sim 5 - \sim 100$ days. However, such trends are not ubiquitous. For $Fe\ K_{\alpha}$ lines originating far from the central corona, one would expect to see an increase in number or strength of continuum–line correlations as one goes towards towards long time scales. However, there is no evidence from the current sample to support this.

The lack of correlation between the continuum and the line suggests that modification to this straightforward picture is required. One possible explanation for the reduced variability in the line relative to the continuum is that a portion of line emission originating in the inner disk is absent or suppressed. The inner portions of the accretion disk may be truncated, highly ionized, or radiatively inefficient (e.g., as in an advection-dominated accretion flow; Narayan & Yi 1994). Geometry may play a role: a relatively more concave disk, for instance, can reprocess a larger fraction of continuum photons in its outer regions (Blackman 1999). For cases in which the bulk of the observed line flux originates in the outer disk, the direct response of the line peak to rapid continuum variations is reduced. Another possibility is that if the X-ray continuum emission is produced in a corotating flare some height

above the reflecting disk, then the orbital motions of the flare and disk can also lead to complex temporal behavior in the observed line flux (Ruszkowski 2000). Fabian & Vaughan (2003) suggested that light-bending near the black hole can lead to substantial de-coupling of the observed continuum and line fluxes. This happens because much of the emission from the X-ray source is focussed on to the disc whereas only a small fraction is able to reach the observer. In such a scenario small changes in the geometry of the X-ray source can lead to relatively large changes in the amount of continuum radiation reaching the observer (hence the strong continuum variations) but relatively little change in the total amount of radiation illuminating the disk.

Another intriguing possibility relies on the presence of an ionized skin on the disk surface. Thermal instabilities can lead to formation of such an ionized skin (Ross, Fabian & Young 1999; Nayakshin, Kazanas & Kallman 2000) with most of the observed neutral line emission originating in the colder layers beneath. The ionized skin can scatter incoming continuum photons and outgoing line photons, affecting the observed neutral line flux, as discussed by Nayakshin (2000) and Nayakshin & Kallman (2001). However, changes in the ionization state of the skin are linked to the dynamic time scale for readjustment of hydrostatic equilibrium (Nayakshin & Kazanas 2002 for a lamppost illuminating model; see also Collin et al. 2003 for a multiple-flare illuminating model). This time scale is usually an order of magnitude or more larger than the light-crossing time; this can be \gtrsim minutes–hours if most of the line emission originates in the inner regions of a typical thin accretion disk (e.g., around a $10^{6-8} M_{\odot}$ black hole). The observed line flux hence may not respond to continuum variations shorter than this time scale, resulting in decorrelation of the observed continuum and line flux variations. Furthermore, the ionization state of the skin depends on the high-energy cutoff of the power-law continuum (Nayakshin & Kallman 2001); this could be variable, but it is difficult to constrain with *RXTE*. Interestingly enough, such a variation in this parameter could lead to a change in $Fe\ K_{\alpha}$ line flux even without a change in 2–10 keV continuum flux. However, recent studies have not been able to directly link the line flux behavior with the ionization state of the disk, e.g., Ballantyne, Vaughan & Fabian (2003).

All of the above scenarios are still consistent with the prediction that both broad and narrow $Fe\ K_{\alpha}$ lines should eventually track continuum variations on time scales of months to years. The finding that the line decreased along with the continuum in the long time scale observation of NGC 5548 is consistent with this idea; however, such correlated behavior is not seen throughout the entire sample. For line emission originating in the outer disk or molecular torus, ionization in the reflecting material is negligible due to the low X-ray continuum flux. However, other processes may be relevant for decorrelating long-term continuum and line variations. For instance, it may be possible for an ionized wind (e.g., George et al. 1998) near the site of reflection to mimic an ionized ‘skin’ in these regions.

5.2. Broadband Spectral Variability

Most of these objects show a strong correlation with no measureable lag between 2–10 keV continuum flux and photon index. Additionally, F_{var} spectra show that in nearly all the objects, the soft-spectrum (narrow line) source Akn 564 being an exception, variability amplitudes tend to increase towards relatively softer energies. These observations show that the broadband emission steepens as it brightens, in line with numerous similar observations (e.g., Magdziarz et al. 1998, Done et al. 2000).

The time-resolved spectral fitting of MCG–6–30–15 performed from *ASCA* data by Shih, Iwasawa & Fabian (2002) and from *XMM-Newton* data by Fabian & Vaughan (2003) point towards a scenario in which flux-correlated changes in the overall 2–10 keV continuum slope are explained by the superposition of a soft, variable power-law likely associated with coronal emission and a harder, much less variable spectral component likely associated with the Compton reflection hump. Taylor, Uttley & McHardy (2003) use flux–flux plots to show that such a description of spectral variability works in MCG–6–30–15 and NGC 3516. Specifically, in this model, the intrinsic slope of the underlying power-law does not vary significantly; rather, it is the *relative contributions* of the two spectral components that change the overall spectral shape as observed. This model does not require physical properties of the power-law emitting corona such as electron temperature, optical depth, or flare size to vary significantly. Furthermore, this two-component model may have relevance to explaining the observed Fe K_{α} variability. As the Fe K_{α} line and Compton hump are expected to originate together, a relatively constant Compton hump could be associated with variability in the Fe K_{α} line that is reduced relative to the continuum variability, as observed (e.g., Shih et al. 2002).

Alternate models to explain the observed spectral variability rely on flux-correlated changes in the power-law slope of the coronal component. In the context of popular thermal Comptonization corona models (Haardt, Maraschi & Ghisellini 1997, Poutanen & Fabian 1999), a flux–photon index correlation can arise if the X-ray variability is due to changes in the input seed photon population. In contrast to the two-component model above, some physical property of the corona may vary with the 2–10 keV X-ray flux in these types of models.

The F_{var} spectra of the soft-spectrum (narrow-line) Seyfert 1 galaxy Akn 564 display a much flatter dependence on energy in the 3.5–9 keV bandpass (and may even be slightly increasing with energy on the long time scales) relative to the other objects, most of which are hard-spectrum (broad-line) Seyfert 1 galaxies. This has been seen previously in Akn 564 by Edelson et al. (2002) as well as in other soft-spectrum sources (Vaughan et al. 2002). This could imply that, in the context of the spectral-pivoting model above, the broadband spectral shape changes very little in soft-spectrum sources, perhaps due to the lack of variation of some physical parameter that does vary in broad-line Seyfert 1 galaxies. Alternatively, if the two-component model above is relevant, it is possible that soft-spectrum sources have much weaker hard/constant components, leading to relatively little change in the overall spectral shape with flux. Overall, however, it is difficult to present a simple, unified phenomenological model to simultaneously explain the dependence

on energy of the variability in broad-line Seyfert 1 galaxies and lack thereof in narrow-line Seyfert 1 galaxies.

6. CONCLUSIONS

Time-resolved broadband spectral fitting has been systematically performed on near-continuous *RXTE* monitoring data of seven Seyfert 1 galaxies in order to probe the behavior of emission components on time scales of both ~days to ~weeks and ~months to ~years. Fe K_{α} line variability is present at a variety of levels. It is readily detectable in some observations; for instance, the average peak-to-trough variations are a factor of ~2 and as high as ~3 in three cases (the short-term observation MCG–6–30–15 (II) and the long-term observations of NGC 4151 and NGC 5548). In other observations, the line does not display appreciably variability; peak-to-trough variations are only ~40–50%. The measured values of F_{var} indicate that a higher fraction of the objects sampled show detectable line variability towards longer time scales. Of particular interest are systematic long-term decreases in line flux over durations of 3–4 years in NGC 3516, NGC 4151, and most notably NGC 5548. Furthermore, the fractional variability amplitude of the line increases towards longer time scales in many objects, “tracking” the red-noise continuum. However, fractional variability amplitudes show that the line does not vary as strongly as the continuum. F_{var} spectra also generally show a dilution in ~5–7 keV continuum variability due to the relatively less variable Fe K_{α} line. In NGC 5548, the continuum and line simultaneously decrease by similar factors over a 4-year period; the long-term observations of NGC 3516 and NGC 4151 also show somewhat similar trends in continuum and line flux. For the sample as a whole, however, there appears to be no simple temporal relation between the continuum and the line, contradicting simple models in which the line flux is driven solely by continuum variations. Local effects such as an ionized skin may be relevant in decorrelating the continuum and line variations, particularly for lines originating in the inner accretion disk. The strongest statement that can be made on the basis of these results is that for most of the Seyfert 1 galaxies studied, the Fe K_{α} emission is less variable than the continuum, and in those cases where there does appear to be evidence for changes in the line flux, these changes are not well correlated with the continuum.

There is evidence for a correlation with no measurable lag between continuum flux and measured photon index on both time scales in many sources. Relatively less model-dependent F_{var} spectra generally show the broadband continua to be more variable at relatively softer energies, supporting Seyfert 1 galaxies’ softening as they brighten, though the soft-spectrum source Akn 564, with its flat F_{var} spectra, is an exception.

The authors acknowledge the dedication of the entire *RXTE* mission team. The authors thank Sergei Nayakshin for suggestions and discussion on ionized skin models, as well as the referee for useful comments. This work has made use of data obtained through the High Energy Astrophysics Science Archive Research Center Online Service, provided by the NASA Goddard Space Flight Center, the TARTARUS database, which is supported by Jane

Turner and Kirpal Nandra under NASA grants NAG 5-7385 and NAG 5-7067, and the NASA/IPAC Extragalactic Database which is operated by the Jet Propulsion Laboratory, California Institute of Technology, under contract

with the National Aeronautics and Space Administration. A.M. & R.E. acknowledge financial support from NASA grant NAG 5-9023.

APPENDIX

NOTES ON INDIVIDUAL SOURCES

- 3C 390.3: The short time scale time-resolved and time-average fit results are in reasonable agreement with Gliozzi et al. (2003): the light curve for Γ has absolute values slightly systematically lower by $\lesssim 0.1$ than Gliozzi et al. (2003) but the variability patterns are identical. On short time scales, a decrease in F_{2-10} by a factor of ~ 2 over a span of 30 days does not appear to have any simultaneous effect on $F_{K\alpha}$, which remains nearly constant during the observation. On long time scales, there is a doubling in F_{2-10} over 300 days, and an increase of $\sim 50\%$ in $F_{K\alpha}$ over approximately the same period.
- MCG-6-30-15: Due to improved background models, the current analysis yields a lower absolute value for R for the integrated spectrum of the short time scale observation MCG-6-30-15 (I) than in VE01 (values of R obtained from spectral fitting are highly sensitive to the shape of the modelled background spectrum above ~ 10 keV), but the time-resolved spectral analysis and the cross-correlation analysis on the short time scale observation MCG-6-30-15 (I) is in excellent agreement with VE01. $F_{K\alpha}$ shows variability on short time scales, as well as in the long time scale observation MCG-6-30-15 (I). The long time scale observation MCG-6-30-15 (II) does not yield a significant detection of variability in the line; one possibility is that on these time scales probed (~ 100 d to ~ 2000 d) the variability is “averaged out” to some degree. There are examples in these observations of large increases or decreases in F_{2-10} (in some cases by a factor of ~ 2) that do not have any obvious immediate effect on $F_{K\alpha}$. The 6.4 keV dips in the F_{var} spectra are prominent, especially for the short time scale observation MCG-6-30-15 (I). The four observations, when considered in order of increasing duration, do not show any obvious pattern to the Fe $K\alpha$ line variability.
- NGC 3516: On short time scales, F_{2-10} and $F_{K\alpha}$ exhibit uncorrelated variability. Persistent trends in F_{2-10} such as the rapid decrease from Modified Julian Day (MJD) 50550–50554 are not simultaneously matched by similar behavior in $F_{K\alpha}$. Rapid changes in $F_{K\alpha}$ occur without sudden changes in F_{2-10} , e.g., the decrease in $F_{K\alpha}$ by $\sim 20\%$ at MJD 50551 and also the increase in $F_{K\alpha}$ by $\sim 30\%$ at MJD 50558 as illustrated in Figure 7. The 6.4 keV dip in the short time scale F_{var} spectra is especially noticeable. On long time scales, both F_{2-10} and $F_{K\alpha}$ show an overall decrease by a factor of ~ 2 over the 1000-day duration.
- NGC 3783: Formally, $F_{K\alpha}$ does not demonstrate appreciable variability on either time scale. Relatively rapid changes in F_{2-10} by $\gtrsim 10\%$ towards the middle of the short time scale observation and $\sim 20\% - \sim 40\%$ towards the beginning and end of the long time scale observation do not appear to have any major simultaneous impact on $F_{K\alpha}$.
- NGC 4151: On short time scales, $F_{K\alpha}$ is not formally variable. One note of interest, for instance, is the doubling of F_{2-10} during the last 4 days of the short time scale observation while $F_{K\alpha}$ remains virtually constant during that time. The 6.4 keV dip in the short time scale F_{var} spectra is especially noticeable. On the long time scale, $F_{K\alpha}$ is much more variable. There are similar decreasing trends by a factor of ~ 3 in both the continuum and line over the whole 800-day duration. Of note is the sudden dip and rise in the line around MJD 51620 in the long time scale observation while F_{2-10} remains nearly constant; Figure 7 demonstrates the dip.
- NGC 5548: On long time scales, a gradual decreasing trend by a factor of 3–4 dominates the behavior of both F_{2-10} and $F_{K\alpha}$. The Fe $K\alpha$ line variability amplitude is substantially larger on the long time scale than the short due to this dominating long time scale trend.
- NGC 7469: All the time-average and time-resolved spectral fit results and cross-correlation results are in reasonable agreement with Nandra et al. (2000). The current analysis yields absolute values of Γ that are slightly systematically lower by $\lesssim 0.1$ and the absolute values of $F_{K\alpha}$ obtained in the current analysis are systematically $\sim 30\%$ higher compared to Nandra et al. (2000), but the variability patterns are consistent.

REFERENCES

Arnaud, K. 1996, in *Astronomical Data Analysis Software and Systems*, Jacoby, G., Barnes, J., eds., ASP Conf. Series Vol. 101, p. 17

Balalntyne, D.R., Vaughan, S. & Fabian, A.C. 2003, MNRAS, 342, 239

Blackman, E. 1999, MNRAS, 306, L25

Blustin, A. et al. 2002, A&A, 392, 453

Blustin, A. et al. 2003, A&A, 403, 473

Chiang, J. et al. 1999, ApJ, 528, 292

Collin, S. et al. 2003, A&A, 400, 437

Done, C. et al. 2000, ApJ, 536, 213

Edelson, R. & Krolik, J. 1988, ApJ, 333, 646

Edelson, R. & Nandra, K. 1999, ApJ, 514, 682

Edelson, R., Griffiths, G., Markowitz, A., Sembay, S., Turner, M.J.L., Warwick, R., 2001, ApJ, 554, 274

Edelson, R., Turner, J., Pounds, K., Vaughan, S., Markowitz, A., Marshall, H., Dobbie, P., Warwick, R. 2002, ApJ, 568, 610

Fabian, A.C., Nandra, K., Reynolds, C.S., Brandt, W.N., Otani, C., Tanaka, Y., Inoue, H., Iwasawa, K. 1995, MNRAS, 277, L11

Fabian, A.C., Vaughan, S., Nandra, K., Iwasawa, K., Ballantyne, D.R., Lee, J.C., De Rosa, A., Turner, A., & Young, A. J. 2002, MNRAS, 335, L1

Fabian, A. & Vaughan, S. 2003, MNRAS, 340, L28

George, I.M. & Fabian, A.C. 1991, MNRAS, 249, 352

George, I.M., Turner, T.J., Netzer, H., Nandra, K., Mushotzky, R. & Yaqoob, T. 1998, ApJS, 114, 73

Gliozzi, M., Sambruna, R., Eracleous, M. 2003, ApJ, 584, 176

Guilbert, P. & Rees, M., 1988, MNRAS, 233, 475

Haardt, F., Maraschi, L. & Ghisellini, G. 1994, ApJ, 432, L95

Haardt, F., Maraschi, L. & Ghisellini, G. 1997, ApJ, 476, 620

Iwasawa, K. et al. 1996, MNRAS, 282, 1038

Iwasawa, K. et al. 1999, MNRAS, 306, L19

Kaspi, S. et al. 2000, ApJ, 533, 631

Kaspi, S. et al. 2001, ApJ, 554, 216

Kaspi, S. et al. 2002, ApJ, 574, 643

Laor, A. 1991, ApJ, 376, 90

Lee, J.C., Fabian, A.C., Brandt, W.N., Reynolds, C.S., Iwasawa, K. 1999, MNRAS, 310, 973

Lee, J. C., Fabian, A.C., Brandt, W.N., Reynolds, C.S., Iwasawa, K. 2000, MNRAS, 318, 857

Magdziarz, P. & Zdziarski, A. 1995, MNRAS, 273, 837

Magdziarz, P. et al. 1998, MNRAS, 301, 179

Maoz, D., Edelson, R. & Nandra, K., 2000, AJ, 119, 119

Maoz, D., Markowitz, A., Edelson, R. & Nandra, K., 2002, AJ, 124, 1988

Markowitz, A. & Edelson, R. 2001, ApJ, 547, 684

Markowitz, A. et al. 2003, ApJ, 593, 96

Matt, G. & Perola, C. 1992, MNRAS, 259, 433

Nandra, K., Pounds, K. & Stewart, G. 1990, MNRAS 242, 660

Nandra, K., George, I.M., Mushotzky, R., Turner, T.J., Yaqoob, T. 1997, ApJ, 476, 70

Nandra, K., George, I.M., Mushotzky, R., Turner, T.J., Yaqoob, T. 1999, ApJ, 523, L17

Nandra, K., Le, T., George, I.M., Edelson, R., Mushotzky, R., Peterson, B., Turner, T.J. 2000, ApJ, 544, 734

Nandra, K. 2001, in "Workshop on X-ray Spectroscopy of AGN with Chandra and XMM-Newton," MPE Report 279, p. 35

Narayan, R. & Yi, I. 1994, ApJL, 428, L13

O'Brien, P. et al. 2001, in "Workshop on X-ray Spectroscopy of AGN with Chandra and XMM-Newton," MPE Report 279, p. 77

Nayakshin, S. 2000, ApJ, 540, L37

Nayakshin, S. & Kallman, T. 2001, ApJ, 546, 406

Nayakshin, S., Kazanas, D. & Kallman, T. 2000, ApJ, 537, 833

Nayakshin, S. & Kazanas, D., 2002, ApJ, 567, 85

Nicastro et al. 2000, ApJ, 536, 718

Peterson, B. et al. 1998, PASP, 110, 660

Petrucci, P. et al. 2002, A&A, 388, L5

Pounds, K. et al. 2003, MNRAS, 341, 953

Poutanen, J. & Fabian, A.C. 1999, MNRAS, 306, L31

Reeves, J. 2002, in *Active Galactic Nuclei: from Central Engine to Host Galaxy*, Eds.: S. Collin, F. Combes and I. Shlosman, PASP (astro-ph/0211381)

Reynolds, C.S. 1997, ApJ, MNRAS, 286, 513

Reynolds, C.S. 2000, ApJ, 533, 811

Ross, R., Fabian, A.C. & Young, A. 1999, MNRAS, 306, 461

Ruszkowski, M. 2000, MNRAS, 315, 1

Schurch, N. & Warwick, R. 2002, MNRAS, 334, 811

Schurch, N., Warwick, R., Griffiths, R. & Ptak, A. 2002, in 'New Visions of the Universe in the XMM-Newton and Chandra Era' conference, astro-ph/0202093

Shih, D.C., Iwasawa, K. & Fabian, A.C. 2002, MNRAS, 333, 687

Stella, L., 1990, Nature, 344, 747

Swank, J. 1998, in Nuclear Phys. B (Proc. Suppl.): The Active X-ray Sky: Results From BeppoSAX and Rossi-XTE, Rome, Italy, 1997 October 21-24, eds. L. Scarsi, H. Bradt, P. Giommi, & F. Fiore, Nucl. Phys. B Suppl. Proc. (The Netherlands: Elsevier Science B.V.), 69, 12

Tanaka, Y., Nandra, K., Fabian, A.C., Inoue, H., Otani, C., Dotani, T., Hayashida, K., Iwasawa, K., Kii, T., Kunieda, H., Makino, F., & Matsuoka, M. 1995, Nature, 375, 659

Taylor, R., Uttley, P., McHardy, I. 2003, MNRAS, in press (astro-ph/0304523)

Turner, T.J. et al. 2002, ApJ, 574, L123

Uttley, P., McHardy, I. & Papadakis, I. 2002, MNRAS, 332, 231

Vaughan, S., Pounds, K., Reeves, J., Warwick, R., Edelson, R. 1999, MNRAS, 304, L34

Vaughan, S. & Edelson, R., 2001, ApJ, 548, 694

Vaughan, S., Boller, Th., Fabian, A., Ballantyne, D.R., Brandt, W. N., Trümper, J., 2002, MNRAS, 337, 247

Vaughan, S., Edelson, R., Warwick, R. & Uttley, P. 2003, MNRAS, submitted

Weaver, K., Gelbord, J. & Yaqoob, T. 2001, ApJ, 550, 261

Welsh, W. 1999, PASP, 111, 1347

White, R. & Peterson, B.M. 1994, PASP, 106, 879

Wilms, J. et al. 2001, MNRAS, 328, L27

Yaqoob, T., Serlemitsos, P.J., Turner, T.J., George, I.M. & Nandra, K. 1996, ApJ, 470, L27

Yaqoob, T. et al. 2001, ApJ, 546, 759

Yaqoob, T., George, I.M. & Turner, T.J. 2001, In Proceedings of "High Energy Universe at Sharp Focus: Chandra Science", Eds. Eric M. Schlegel and Saequ Vrtilek (astro-ph/0111428)

TABLE 1
SOURCE AND SAMPLING PARAMETERS

| Source Name | 2–10 keV Lum. (log(erg s ⁻¹)) | z | MJD Date Range | Mean c s ⁻¹ | Spectral Fits Time Bin | Spectral Fits No. Pts |
|----------------|---|-------|-----------------|------------------------|------------------------|-----------------------|
| 3C 390.3 | 44.26 | 0.056 | 50220.6–50278.0 | 2.3 | 6.0 d | 10 |
| MCG–6–30–15 I | 42.80 | 0.008 | 50664.1–50672.5 | 4.1 | 0.13 d | 63 |
| MCG–6–30–15 II | 42.83 | 0.008 | 51622.7–51676.0 | 4.4 | 1.6 d | 34 |
| NGC 3516 | 42.90 | 0.009 | 50523.0–50657.4 | 4.2 | 6.4 d | 21 |
| NGC 3783 | 43.12 | 0.010 | 51960.1–51980.0 | 5.7 | 1.7 d | 12 |
| NGC 4151 | 42.24 | 0.003 | 51870.6–51904.9 | 7.4 | 1.4 d | 24 |
| NGC 5548 | 43.52 | 0.017 | 52091.6–52126.7 | 4.5 | 3.2 d | 11 |
| NGC 7469 | 43.25 | 0.016 | 50244.0–50275.7 | 2.8 | 1.3 d | 25 |
| 3C 390.3 | 44.40 | 0.056 | 51186.0–51964.8 | 3.2 | 51.9 d | 15 |
| MCG–6–30–15 I | 42.81 | 0.008 | 51926.7–52252.9 | 4.2 | 23.4 d | 13 |
| MCG–6–30–15 II | 42.85 | 0.008 | 50159.8–52252.9 | 4.6 | 128.7 d | 16 |
| NGC 3516 | 42.86 | 0.009 | 50523.0–51593.4 | 3.8 | 53.5 d | 20 |
| NGC 3783 | 43.22 | 0.010 | 51180.5–52375.2 | 7.1 | 59.8 d | 20 |
| NGC 4151 | 42.55 | 0.003 | 51179.6–51964.6 | 14.9 | 43.6 d | 18 |
| NGC 5548 | 43.55 | 0.017 | 51183.9–52643.1 | 4.8 | 104.2 d | 14 |

Note. — The short time scale data are listed in the top half of the table; the bottom half lists the long time scale data. Column (2), log of the 2–10 keV luminosity, was calculated using the online W3PIMMS tool and using the mean 2–10 keV count rate per PCU, X-ray photon indices and neutral absorption based on the time-averaged spectral fitting below, and assuming $H_0 = 75$ km s⁻¹ Mpc⁻¹ and $q_0 = 0.5$. The count rates in Column (5) are 2–10 keV count rates per PCU.

TABLE 2
TIME-AVERAGE FIT PARAMETERS, SINGLE-GAUSSIAN MODEL

| Source Name | N_{H} | Γ | E_o (keV) | σ (keV) | $F_{K\alpha}$ | R | $\chi^2/\text{d.o.f.}$ |
|----------------|----------------|---------------------------|------------------------|------------------------|------------------------|------------------------|------------------------|
| 3C 390.3 | 4.28 | 1.641 ± 0.006 | $6.00^{+0.04}_{-0.06}$ | 0.44 ± 0.07 | 0.64 ± 0.06 | < 0.03 | 61.0/34 |
| MCG-6-30-15 I | 4.09 | 2.018 ± 0.010 | 5.87 ± 0.02 | 0.68 ± 0.02 | 1.79 ± 0.06 | 0.85 ± 0.07 | 292.0/33 |
| MCG-6-30-15 II | 4.09 | 1.947 ± 0.016 | $6.17^{+0.02}_{-0.03}$ | 0.46 ± 0.04 | 1.35 ± 0.07 | 1.15 ± 0.12 | 23.0/27 |
| NGC 3516 | 2.94 | 1.573 ± 0.007 | 6.02 ± 0.01 | $0.59^{+0.01}_{-0.02}$ | $2.62^{+0.06}_{-0.04}$ | $0.20^{+0.04}_{-0.07}$ | 487.6/33 |
| NGC 3783 | 8.26 | $1.666^{+0.022}_{-0.019}$ | $6.27^{+0.04}_{-0.03}$ | 0.41 ± 0.06 | 1.75 ± 0.12 | 0.62 ± 0.12 | 22.3/28 |
| NGC 4151 | 616 | 1.524 ± 0.010 | 6.40 ± 0.01 | $0.14^{+0.04}_{-0.03}$ | 3.45 ± 0.08 | 0.55 ± 0.05 | 101.0/26 |
| NGC 5548 | 1.75 | 1.733 ± 0.017 | 6.27 ± 0.06 | 0.42 ± 0.10 | $0.73^{+0.07}_{-0.08}$ | 0.44 ± 0.10 | 25.3/28 |
| NGC 7469 | 4.86 | 1.845 ± 0.009 | 6.31 ± 0.02 | 0.28 ± 0.04 | 0.64 ± 0.02 | 0.42 ± 0.05 | 146.0/33 |
| 3C 390.3 | 4.28 | $1.646^{+0.012}_{-0.008}$ | 6.10 ± 0.04 | $0.25^{+0.08}_{-0.11}$ | 0.47 ± 0.04 | $0.03^{+0.06}_{-0.02}$ | 122.0/97 |
| MCG-6-30-15 I | 4.09 | $2.020^{+0.030}_{-0.029}$ | $5.92^{+0.07}_{-0.08}$ | $0.75^{+0.10}_{-0.09}$ | 1.76 ± 0.02 | $1.96^{+0.28}_{-0.25}$ | 30.75/28 |
| MCG-6-30-15 II | 4.09 | 2.000 ± 0.006 | 6.00 ± 0.01 | $0.59^{+0.01}_{-0.02}$ | 1.75 ± 0.03 | $1.17^{+0.05}_{-0.04}$ | 726.9/98 |
| NGC 3516 | 2.94 | $1.642^{+0.005}_{-0.004}$ | 6.09 ± 0.01 | $0.47^{+0.02}_{-0.01}$ | 2.11 ± 0.03 | 0.27 ± 0.03 | 1009.7/65 |
| NGC 3783 | 8.26 | $1.693^{+0.008}_{-0.007}$ | 6.23 ± 0.02 | 0.43 ± 0.03 | 2.04 ± 0.06 | $0.47^{+0.05}_{-0.04}$ | 206.6/98 |
| NGC 4151 | 812 | $1.692^{+0.014}_{-0.005}$ | $6.40^{+0.05}_{-0.01}$ | $0.12^{+0.02}_{-0.12}$ | $3.72^{+0.04}_{-0.08}$ | $0.55^{+0.04}_{-0.01}$ | 581.6/94 |
| NGC 5548 | 1.75 | 1.739 ± 0.010 | $6.28^{+0.02}_{-0.03}$ | $0.36^{+0.05}_{-0.03}$ | $0.76^{+0.04}_{-0.06}$ | $0.41^{+0.02}_{-0.08}$ | 105.0/99 |

Note. — Results of fits of the model (power-law + PEXRAV + Gaussian) \times absorption to the time-average data for all targets. The short time scale data are listed in the top half of the table; the bottom half lists the long time scale data. The PEXRAV component was omitted for the short time scale spectrum of 3C 390.3. Column (2) lists the neutral absorption column in units of 10^{20} cm^{-2} , modelled using the Galactic column for all sources except NGC 4151. The line energy, E_o , Column (4), is the energy in the observed, not the rest, frame. Column (5) lists σ , the FWHM of the Gaussian. Column (6) lists the Fe $K\alpha$ line normalization in units of $10^{-4} \text{ ph cm}^{-2} \text{ s}^{-1}$. Column (7) lists R , the relative reflection of the Compton reflection hump. Errors listed above are 1σ errors determined by XSPEC.

TABLE 3
TIME-AVERAGE FIT PARAMETERS, LAOR MODEL

| Source Name | N_H | Γ | E_o (keV) | β | R_{in} | $F_{K\alpha}$ | R | $\chi^2/\text{d.o.f.}$ |
|----------------|-------|---------------------------|------------------------|---------------------|---------------------|------------------------|------------------------|------------------------|
| 3C 390.3 | 4.28 | $1.637^{+0.007}_{-0.005}$ | 6.19 ± 0.5 | $3.8^{+6.1}_{-1.0}$ | 13^{+7}_{-6} | $0.68^{+0.06}_{-0.03}$ | < 0.02 | 55.6/33 |
| MCG-6-30-15 I | 4.09 | $1.922^{+0.019}_{-0.015}$ | $6.47^{+0.02}_{-0.03}$ | 3.2 ± 0.1 | $2.2^{+0.8}_{-1.0}$ | $2.76^{+0.22}_{-0.26}$ | 0.45 ± 0.08 | 98.2/32 |
| MCG-6-30-15 II | 4.09 | $1.932^{+0.018}_{-0.016}$ | 6.34 ± 0.3 | $3.6^{+2.1}_{-0.7}$ | 13^{+6}_{-4} | 1.37 ± 0.07 | 1.06 ± 0.12 | 19.6/25 |
| NGC 3516 | 2.94 | 1.507 ± 0.004 | $6.48^{+0.01}_{-0.03}$ | $8.0^{+1.9}_{-1.1}$ | $7.1^{+1.1}_{-0.1}$ | 3.09 ± 0.04 | < 0.03 | 101.5/32 |
| NGC 3783 | 8.26 | 1.650 ± 0.022 | 6.46 ± 0.5 | $2.5^{+0.1}_{-0.4}$ | $5.8^{+4.8}_{-4.2}$ | $1.95^{+0.27}_{-0.37}$ | $0.57^{+0.06}_{-0.19}$ | 20.4/27 |
| NGC 4151 | 618 | $1.524^{+0.011}_{-0.008}$ | 6.42 ± 0.1 | $3.0^{+6.9}_{-3.0}$ | 300^{+100}_{-275} | $3.43^{+0.10}_{-0.06}$ | 0.55 ± 0.05 | 101.0/25 |
| NGC 5548 | 1.75 | $1.725^{+0.017}_{-0.025}$ | $6.43^{+0.15}_{-0.07}$ | $2.8^{+7.1}_{-0.8}$ | $8.7^{+24}_{-7.5}$ | $0.78^{+0.32}_{-0.11}$ | $0.40^{+0.10}_{-0.09}$ | 24.5/27 |
| NGC 7469 | 4.86 | 1.832 ± 0.008 | 6.43 ± 0.2 | 2.2 ± 0.1 | 2.8 ± 1.4 | $0.79^{+0.08}_{-0.03}$ | $0.38^{+0.03}_{-0.06}$ | 117.4/32 |
| 3C 390.3 | 4.28 | $1.653^{+0.001}_{-0.002}$ | 6.12 ± 0.4 | $8.2^{+1.7}_{-8.1}$ | 260^{+140}_{-200} | $0.44^{+0.02}_{-0.03}$ | $0.06^{+0.06}_{-0.01}$ | 122.1/96 |
| MCG-6-30-15 I | 4.09 | $1.975^{+0.021}_{-0.030}$ | 6.41 ± 0.9 | $9.9^{+0.0}_{-6.9}$ | $8.9^{+1.0}_{-2.3}$ | $1.70^{+0.15}_{-0.10}$ | $1.59^{+0.22}_{-0.07}$ | 27.1/27 |
| MCG-6-30-15 II | 4.09 | $1.919^{+0.005}_{-0.010}$ | $6.43^{+0.01}_{-0.02}$ | 2.9 ± 0.1 | $1.8^{+0.4}_{-0.5}$ | $2.64^{+0.01}_{-0.07}$ | $0.81^{+0.03}_{-0.05}$ | 457.0/97 |
| NGC 3516 | 2.94 | 1.582 ± 0.002 | 6.37 ± 0.1 | 2.6 ± 0.1 | $2.8^{+0.1}_{-0.2}$ | $2.73^{+0.02}_{-0.09}$ | 0.08 ± 0.02 | 766.8/64 |
| NGC 3783 | 8.26 | $1.664^{+0.003}_{-0.009}$ | $6.43^{+0.03}_{-0.02}$ | $2.9^{+0.2}_{-0.1}$ | 6.3 ± 0.8 | $2.37^{+0.17}_{-0.03}$ | 0.38 ± 0.03 | 185.4/97 |
| NGC 4151 | 690 | $1.604^{+0.010}_{-0.011}$ | 6.39 ± 0.1 | $0.0^{+9.9}_{-0.0}$ | 230^{+170}_{-60} | $4.04^{+0.1}_{-0.2}$ | $0.54^{+0.02}_{-0.03}$ | 450.5/91 |
| NGC 5548 | 1.75 | 1.732 ± 0.011 | 6.38 ± 0.3 | $8.6^{+1.3}_{-5.3}$ | 44^{+1}_{-25} | $0.73^{+0.04}_{-0.03}$ | $0.40^{+0.05}_{-0.03}$ | 120.5/97 |

Note. — Fit parameters for the Laor model fits to the time-averaged data. The short time scale data are listed in the top half of the table; the bottom half lists the long time scale data. The PEXRAV component was omitted for the short time scale spectra of 3C 390.3 and NGC 3516. Column (2) lists the neutral absorption column in units of 10^{20} cm^{-2} , modelled using the Galactic column for all sources except NGC 4151. Column (4) is the emissivity index β . Column (5) is R_{in} , the innermost disk radius of line emission, in units of GM/c^2 where M is the black hole mass. Column (7) lists the Fe $K\alpha$ line normalization in units of $10^{-4} \text{ ph cm}^{-2} \text{ s}^{-1}$. Column (8) lists R , the relative reflection of the Compton reflection hump. Errors listed above are 1σ errors determined by XSPEC.

TABLE 4
F-TEST RESULTS TO THAW Γ , $F_{K\alpha}$ OR R IN THE SINGLE-GAUSSIAN MODEL

| Source Name | Γ F | Γ Prob | $F_{K\alpha}$ F | $F_{K\alpha}$ Prob | R F | R Prob |
|----------------|---------------|----------------------|--------------------|-----------------------|----------|-------------|
| 3C 390.3 | 5.8 | 1.2E-10 | 1.80 | 3.7 E-2 | N/A | N/A |
| MCG-6-30-15 I | 1.78 | 1.9E-4 | 1.63 | 1.4E-3 | 0.76 | 0.92 |
| MCG-6-30-15 II | 2.4 | 1.6E-5 | 1.70 | 5.7E-3 | 1.31 | 0.11 |
| NGC 3516 | 24.5 | $<1 \times 10^{-40}$ | 3.20 | 2.9E-6 | 0.39 | 0.99 |
| NGC 3783 | 0.81 | 0.64 | 0.72 | 0.74 | 0.53 | 0.90 |
| NGC 4151 | 1.94 | 4.8E-3 | 0.82 | 0.71 | 1.04 | 0.41 |
| NGC 5548 | 1.5 | 0.26 | 0.99 | 0.45 | 0.47 | 0.92 |
| NGC 7469 | 3.80 | 1.7E-9 | 2.05 | 1.9E-3 | 1.58 | 3.5E-2 |
| 3C 390.3 | 5.84 | 3.2E-11 | 0.94 | 0.52 | 0.65 | 0.84 |
| MCG-6-30-15 I | 2.21 | 2.9E-2 | 1.65 | 4.4E-2 | 1.80 | 2.3E-2 |
| MCG-6-30-15 II | 2.90 | 1.3E-4 | 2.29 | 2.9E-3 | 0.86 | 0.62 |
| NGC 3516 | 13.0 | 2.3E-36 | 4.83 | 3.8E-11 | 1.08 | 0.36 |
| NGC 3783 | 1.17 | 0.28 | 1.03 | 0.43 | 0.53 | 0.95 |
| NGC 4151 | 12.3 | 5.2E-31 | 7.74 | 2.2E-18 | 1.76 | 2.7E-2 |
| NGC 5548 | 1.77 | 4.11E-2 | 1.83 | 3.2E-2 | 0.85 | 0.61 |

Note. — Results of F-test to determine which parameters to thaw in the time-resolved fits. High values of the F-statistic and low values of the probability (of observing that value of F from a random set of data) indicate that the fits show significant improvement to thaw that parameter. The short time scale data are listed in the top half of the table; the bottom half lists the long time scale data.

TABLE 5
MEAN SPECTRAL FIT VARIABILITY PARAMETERS AND ERRORS

| Source Name | Mean F_{2-10} (10^{-11} ph cm $^{-2}$ s $^{-1}$) | Mean Γ | Mean $F_{K\alpha}$ (10^{-4} ph cm $^{-2}$ s $^{-1}$) |
|----------------|---|-------------------|---|
| 3C 390.3 | 2.58 ± 0.05 | 1.633 ± 0.023 | 0.639 ± 0.174 |
| MCG-6-30-15 I | 4.73 ± 0.05 | 2.005 ± 0.063 | 1.829 ± 0.250 |
| MCG-6-30-15 II | 4.58 ± 0.10 | 1.914 ± 0.103 | 1.384 ± 0.261 |
| NGC 3516 | 4.80 ± 0.08 | 1.609 ± 0.061 | 2.384 ± 0.177 |
| NGC 3783 | 6.15 ± 0.14 | 1.665 ± 0.028 | 1.768 ± 0.200 |
| NGC 4151 | 10.11 ± 0.19 | 1.519 ± 0.037 | 3.466 ± 0.264 |
| NGC 5548 | 4.85 ± 0.13 | 1.723 ± 0.028 | 0.724 ± 0.149 |
| NGC 7469 | 3.24 ± 0.05 | 1.845 ± 0.034 | 0.642 ± 0.096 |
| 3C 390.3 | 3.44 ± 0.08 | 1.644 ± 0.044 | 0.453 ± 0.066 |
| MCG-6-30-15 I | 5.10 ± 0.14 | 2.002 ± 0.080 | 1.788 ± 0.253 |
| MCG-6-30-15 II | 5.41 ± 0.10 | 2.014 ± 0.038 | 1.801 ± 0.226 |
| NGC 3516 | 4.31 ± 0.08 | 1.583 ± 0.061 | 1.953 ± 0.269 |
| NGC 3783 | 7.56 ± 0.12 | 1.689 ± 0.037 | 2.080 ± 0.202 |
| NGC 4151 | 22.23 ± 0.24 | 1.616 ± 0.055 | 4.878 ± 0.795 |
| NGC 5548 | 4.12 ± 0.10 | 1.711 ± 0.041 | 0.750 ± 0.104 |

Note. — The short time scale data are listed in the top half of the table; the bottom half lists the long time scale data. Listed are the mean values of F_{2-10} , Γ and $F_{K\alpha}$. Errors for Γ and $F_{K\alpha}$ were derived using the formulation of §3.3. The F_{2-10} errors listed above are the average of the errors for F_{2-10} in a given time bin, which were derived from the 2–10 keV continuum light curve, using the mean flux error on the ~ 1 ks exposures in that time bin.

TABLE 6
 F_{var} VALUES

| Source Name | Time Scale | Continuum F_{var} (%) | Line F_{var} (%) |
|----------------|---------------|----------------------------|-----------------------|
| 3C 390.3 | Short | 29.3 \pm 0.6 | Undef. |
| | Long | 26.9 \pm 0.6 | 13.7 \pm 4.7 |
| MCG-6-30-15 | Short I | 18.5 \pm 0.1 | 9.4 \pm 2.5 |
| | Short II | 17.4 \pm 0.4 | 14.4 \pm 4.4 |
| | Long I | 16.1 \pm 0.7 | 14.1 \pm 4.8 |
| | Long II | 7.0 \pm 0.5 | Undef. |
| NGC 3516 | Short | 24.6 \pm 0.4 | 5.6 \pm 2.2 |
| | Long | 32.9 \pm 0.4 | 14.9 \pm 3.7 |
| NGC 3783 | Short | 4.7 \pm 0.7 | 6.0 \pm 5.5 |
| | Long | 10.0 \pm 0.4 | 1.5 \pm 9.9 |
| NGC 4151 | Short | 16.7 \pm 0.4 | 3.2 \pm 3.1 |
| | Long | 30.5 \pm 0.2 | 24.0 \pm 4.3 |
| NGC 5548 | Short | 24.8 \pm 0.8 | 8.2 \pm 12.6 |
| | Long | 39.0 \pm 0.7 | 28.8 \pm 3.9 |
| NGC 7469 | Short | 13.3 \pm 0.3 | Undef. |

Note. — Undefined fractional variability measurements indicate a measured variance that is smaller than that expected solely from measurement noise.

TABLE 7
 $F_{2-10}-F_{K\alpha}$ CROSS-CORRELATION RESULTS

| Source Name | Time Scale | DCF $\tau(d)$ | DCF r_{max} | ICF $\tau(d)$ | ICF r_{max} |
|----------------|---------------|------------------|------------------|------------------|------------------|
| 3C 390.3 | Short | +12.0 | 0.46 | +9 \pm 20.2 | 0.61 |
| MCG-6-30-15 I | | +1.3 | 0.51 | +1.4 \pm 1.5 | 0.53 |
| MCG-6-30-15 II | | -14.4 | 0.38 | -14.4 \pm 18.0 | 0.38 |
| NGC 3516 | | +6.4 | 0.17 | +6.4 \pm 41.2 | 0.18 |
| NGC 3783 | | +3.3 | 0.59 | +4.1 \pm 5.4 | 0.72 |
| NGC 4151 | | +2.8 | 0.23 | +3.5 \pm 10.0 | 0.27 |
| NGC 5548 | | +6.4 | 0.63 | +8.0 \pm 6.1 | 0.68 |
| NGC 7469 | | 0 | 0.57 | +0.6 \pm 7.2 | 0.67 |
| 3C 390.3 | Long | +51.9 | 0.48 | +25.9 \pm 159 | 0.48 |
| MCG-6-30-15 I | | 0 | 0.75 | 0 \pm 65.6 | 0.73 |
| MCG-6-30-15 II | | -386 | 0.45 | 0 \pm 606 | 0.45 |
| NGC 3516 | | -161 | 0.66 | -134 \pm 262 | 0.71 |
| NGC 3783 | | 0 | 0.53 | 0 \pm 388 | 0.51 |
| NGC 4151 | | 0 | 0.56 | 0 \pm 258 | 0.61 |
| NGC 5548 | | 0 | 0.84 | 0 \pm 428 | 0.87 |

Note. — Lags are defined such that a positive lag means the continuum light curve leads the line light curve.

TABLE 8
 F_{2-10} – Γ CROSS-CORRELATION RESULTS

| Source Name | Time Scale | DCF $\tau(d)$ | DCF r_{max} | ICF $\tau(d)$ | ICF r_{max} |
|----------------|------------|---------------|---------------|-----------------|---------------|
| 3C 390.3 | Short | 0 | 0.91 | -3.0 ± 7.8 | 0.92 |
| MCG–6–30–15 I | | 0 | 0.82 | 0 ± 1.4 | 0.82 |
| MCG–6–30–15 II | | 0 | 0.54 | -0.8 ± 10.9 | 0.57 |
| NGC 3516 | | 0 | 0.90 | 0 ± 10.6 | 0.90 |
| NGC 3783 | | 0 | 0.88 | 0 ± 5.7 | 0.89 |
| NGC 4151 | | 0 | 0.69 | 0 ± 8.4 | 0.73 |
| NGC 5548 | | -9.6 | 0.85 | -8.0 ± 5.3 | 0.88 |
| NGC 7469 | | -3.8 | 0.64 | -4.4 ± 8.4 | 0.73 |
| 3C 390.3 | Long | 0 | 0.85 | 0 ± 136 | 0.82 |
| MCG–6–30–15 I | | 0 | 0.94 | 0 ± 66.6 | 0.86 |
| MCG–6–30–15 II | | 0 | 0.62 | 0 ± 555 | 0.64 |
| NGC 3516 | | 0 | 0.92 | 0 ± 161 | 0.93 |
| NGC 3783 | | 0 | 0.81 | 0 ± 357 | 0.81 |
| NGC 4151 | | 0 | 0.31 | $+21.8 \pm 191$ | 0.46 |
| NGC 5548 | | 0 | 0.74 | -52.1 ± 506 | 0.75 |

Note. — Lags are defined such that a positive lag means the continuum light curve leads the Γ light curve.

TABLE 9
 Γ – $F_{K\alpha}$ CROSS-CORRELATION RESULTS

| Source Name | Time Scale | DCF $\tau(d)$ | DCF r_{max} | ICF $\tau(d)$ | ICF r_{max} |
|----------------|------------|---------------|---------------|------------------|---------------|
| 3C 390.3 | Short | +12.0 | 0.64 | $+9.0 \pm 18.1$ | 0.66 |
| MCG–6–30–15 I | | +1.5 | 0.49 | $+1.4 \pm 2.0$ | 0.54 |
| MCG–6–30–15 II | | +9.6 | 0.38 | $+10.4 \pm 18.2$ | 0.44 |
| NGC 3516 | | -32.0 | 0.25 | -35.2 ± 42.9 | 0.33 |
| NGC 3783 | | +3.3 | 0.70 | $+4.1 \pm 5.6$ | 0.74 |
| NGC 4151 | | +4.2 | 0.28 | $+4.9 \pm 11.6$ | 0.33 |
| NGC 5548 | | +9.6 | 0.43 | $+9.6 \pm 11.3$ | 0.47 |
| NGC 7469 | | +5.7 | 0.40 | $+5.7 \pm 9.6$ | 0.45 |
| 3C 390.3 | Long | +51.9 | 0.52 | $+25.9 \pm 156$ | 0.56 |
| MCG–6–30–15 I | | 0 | 0.67 | -11.7 ± 97.0 | 0.63 |
| MCG–6–30–15 II | | -386 | 0.47 | -386 ± 667 | 0.44 |
| NGC 3516 | | -107 | 0.79 | -134 ± 300 | 0.82 |
| NGC 3783 | | 0 | 0.47 | 0 ± 390 | 0.46 |
| NGC 4151 | | -43.6 | 0.19 | -174 ± 280 | 0.17 |
| NGC 5548 | | 0 | 0.55 | $+52.1 \pm 481$ | 0.61 |

Note. — Lags are defined such that a positive lag means the first light curve leads the second.

TABLE 10
 F_{var} SPECTRAL SAMPLING PARAMETERS

| Source Name | MJD Date Range | Time Bin Size (d) | No. Pts |
|----------------|-----------------|-------------------|---------|
| 3C 120 | 50458.5–50515.3 | 2.0 | 29 |
| 3C 390.3 | 50220.6–50278.0 | 2.0 | 29 |
| Akn 564 | 51694.8–51726.7 | 1.6 | 20 |
| Fairall 9 | 52144.9–52179.0 | 1.6 | 21 |
| IC 4329a | 50665.8–50723.5 | 2.0 | 28 |
| MCG–6-30-15 I | 50664.1–50672.5 | 0.13 | 63 |
| MCG–6-30-15 II | 51622.7–51676.0 | 1.6 | 34 |
| NGC 3516 | 50523.0–50657.4 | 4.8 | 28 |
| NGC 3783 | 51960.1–51980.0 | 0.66 | 30 |
| NGC 4151 | 51870.6–51904.9 | 1.2 | 29 |
| NGC 5548 | 52091.6–52126.7 | 1.3 | 27 |
| NGC 7469 | 50244.0–50275.7 | 1.1 | 30 |
| 3C 120 | 50812.4–51259.7 | 20.4 | 19 |
| 3C 390.3 | 51259.7–51676.0 | 20.8 | 20 |
| Akn 120 | 50868.1–51259.7 | 16.3 | 19 |
| Akn 564 | 51678.7–52683.7 | 50.2 | 20 |
| Fairall 9 | 51679.8–52678.2 | 50.0 | 20 |
| MCG–6-30-15 I | 51926.7–52252.9 | 13.1 | 23 |
| MCG–6-30-15 II | 50188.9–51259.7 | 53.6 | 20 |
| NGC 3516 | 50523.0–51259.7 | 28.3 | 26 |
| NGC 3783 | 51679.7–52375.9 | 29.0 | 24 |
| NGC 4051 | 51676.0–52228.3 | 27.6 | 20 |
| NGC 4151 | 51259.7–51676.0 | 17.3 | 24 |
| NGC 5548 | 51678.7–52681.4 | 45.6 | 22 |

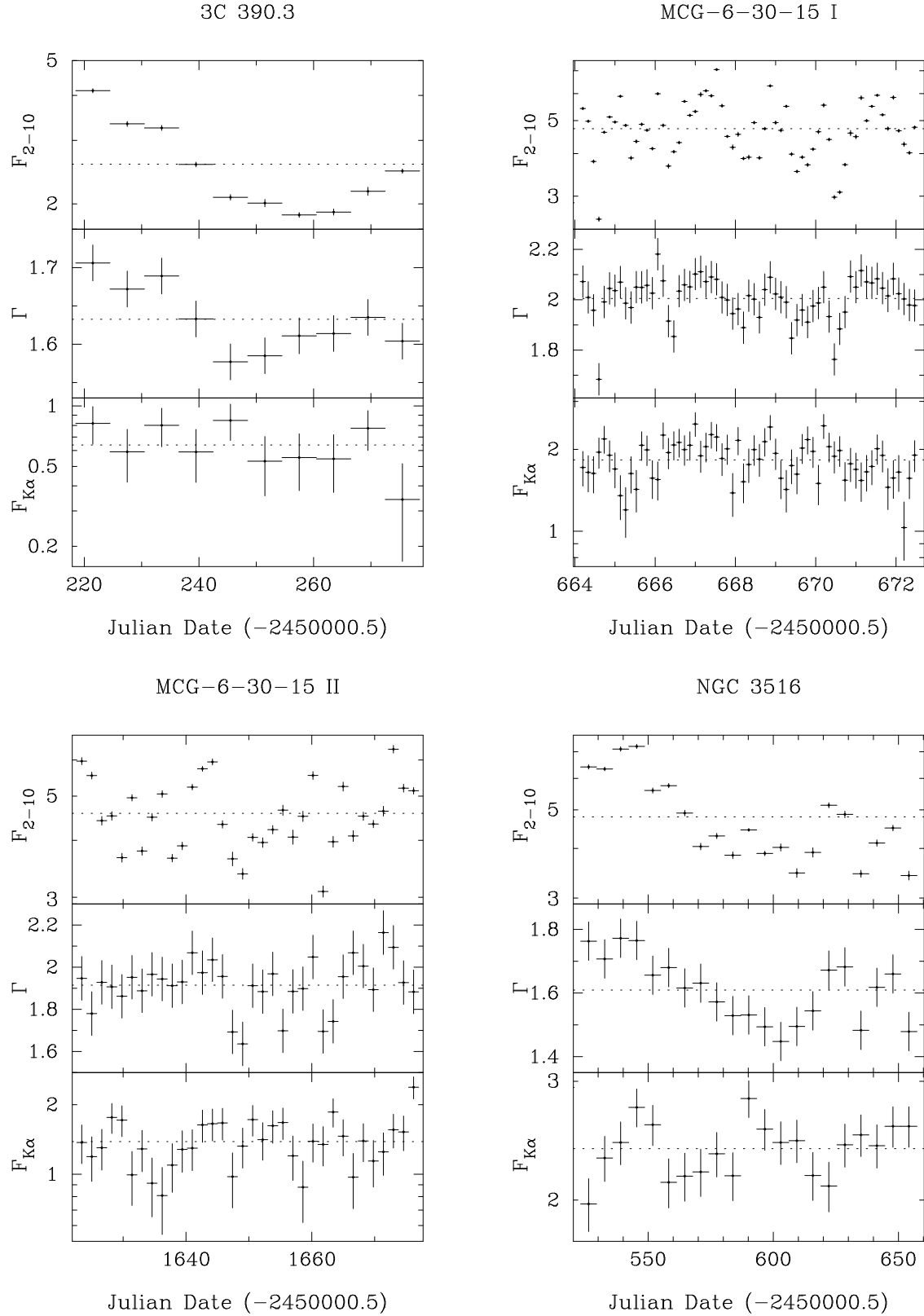


FIG. 1.— Short time scale light curves for continuum flux, Γ and Fe $K\alpha$ line flux. The continuum flux is in units of 10^{-11} photons $cm^{-2} s^{-1}$. The Fe $K\alpha$ flux is in units of 10^{-4} photons $cm^{-2} s^{-1}$. The dotted lines represent the mean values of each parameter.

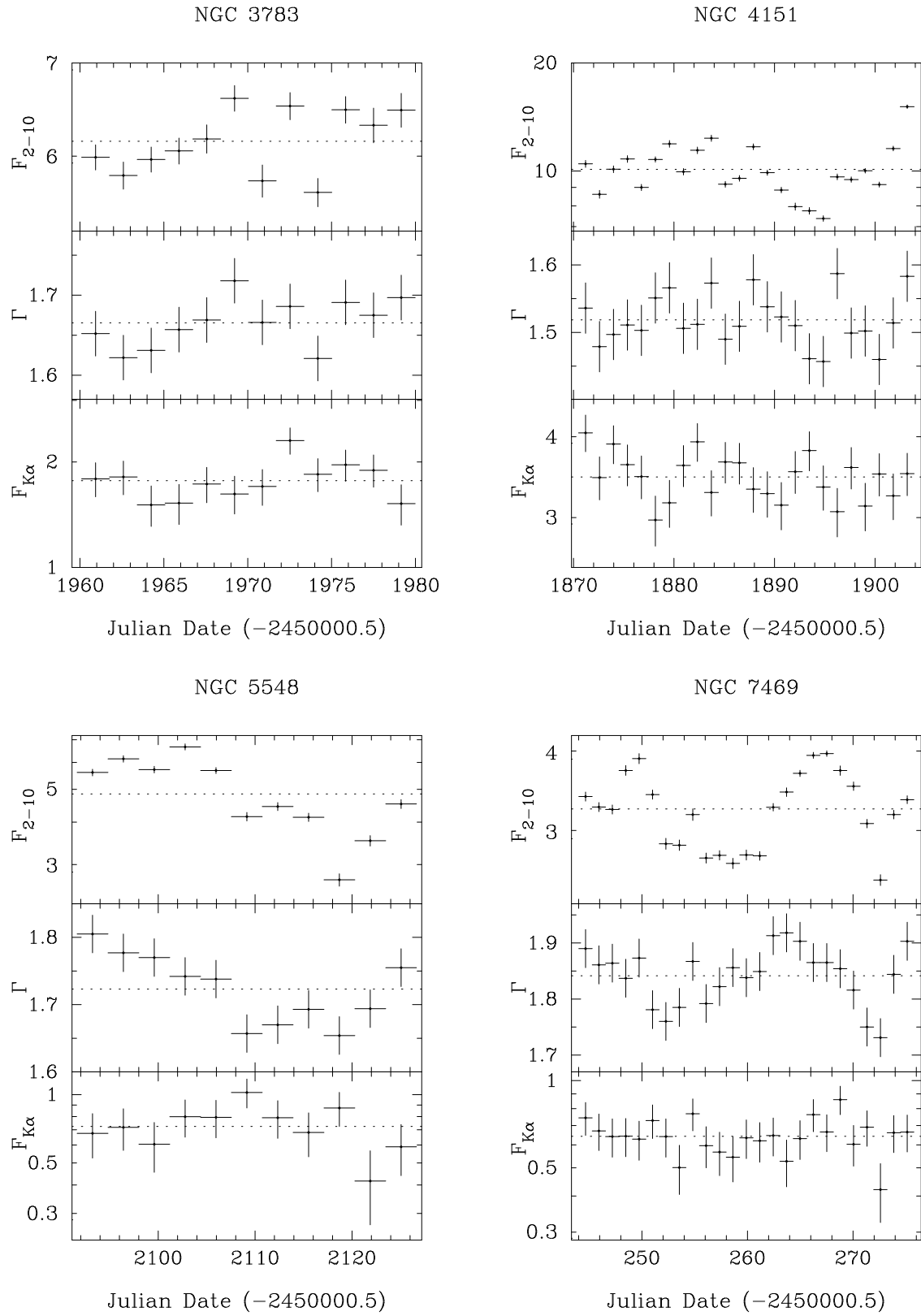


FIG. 1.— Figure 1, cont'd.

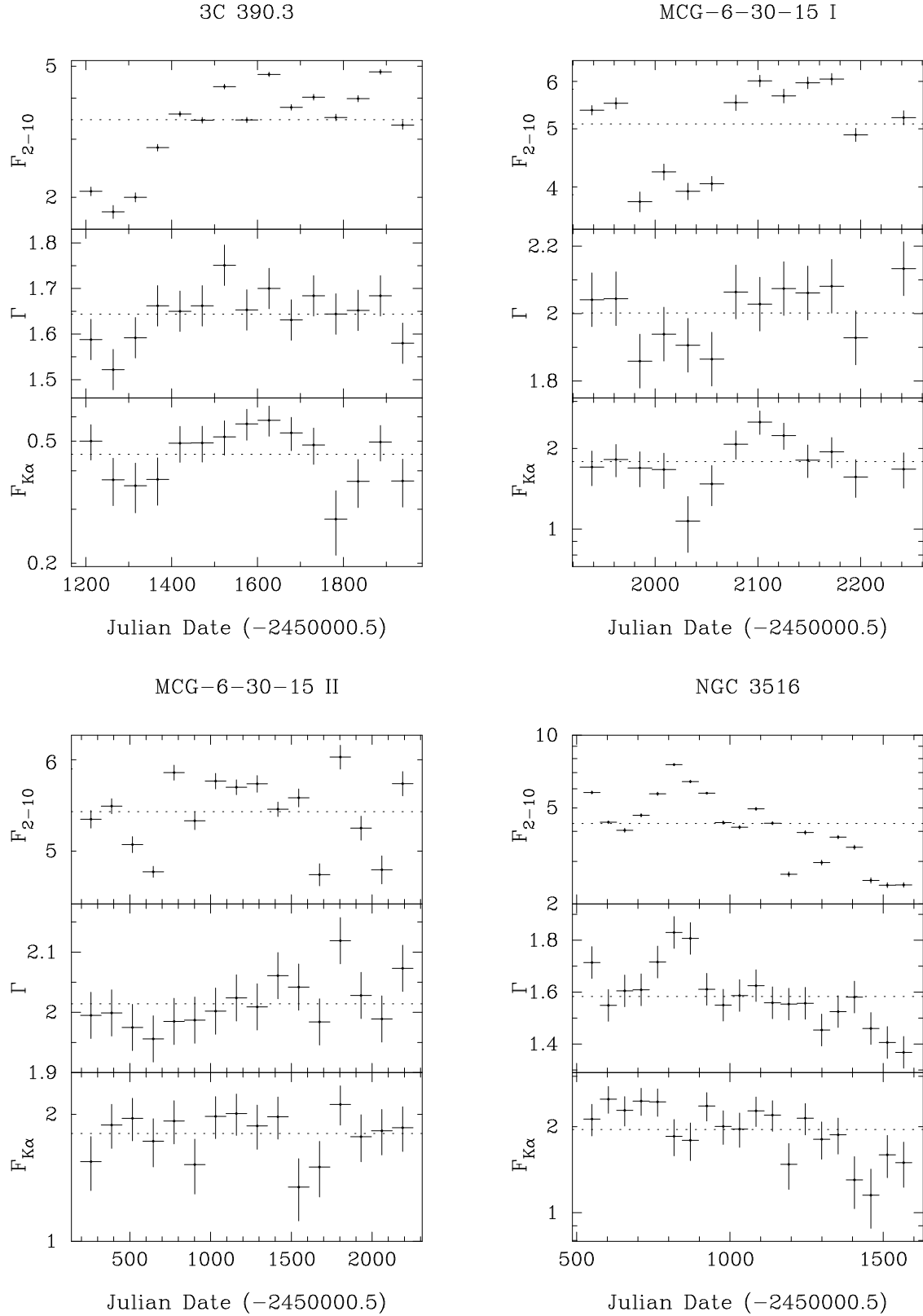


FIG. 2.— Long time scale light curves for continuum flux, Γ and Fe $K\alpha$ line flux. The continuum flux is in units of 10^{-11} photons $\text{cm}^{-2} \text{s}^{-1}$. The Fe $K\alpha$ flux is in units of 10^{-4} photons $\text{cm}^{-2} \text{s}^{-1}$. The dotted lines represent the mean values of each parameter.

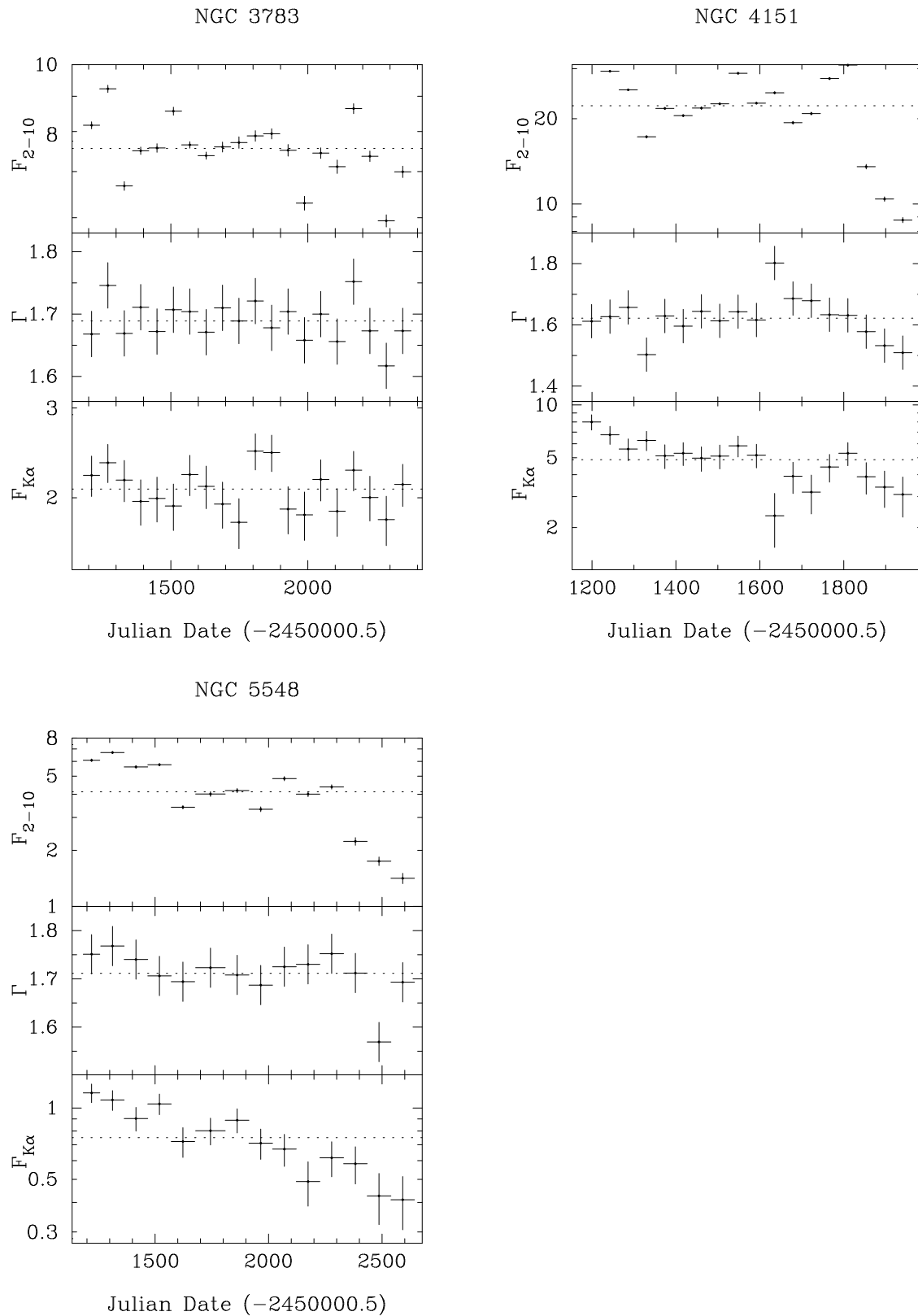


FIG. 2.— Figure 2, cont'd.

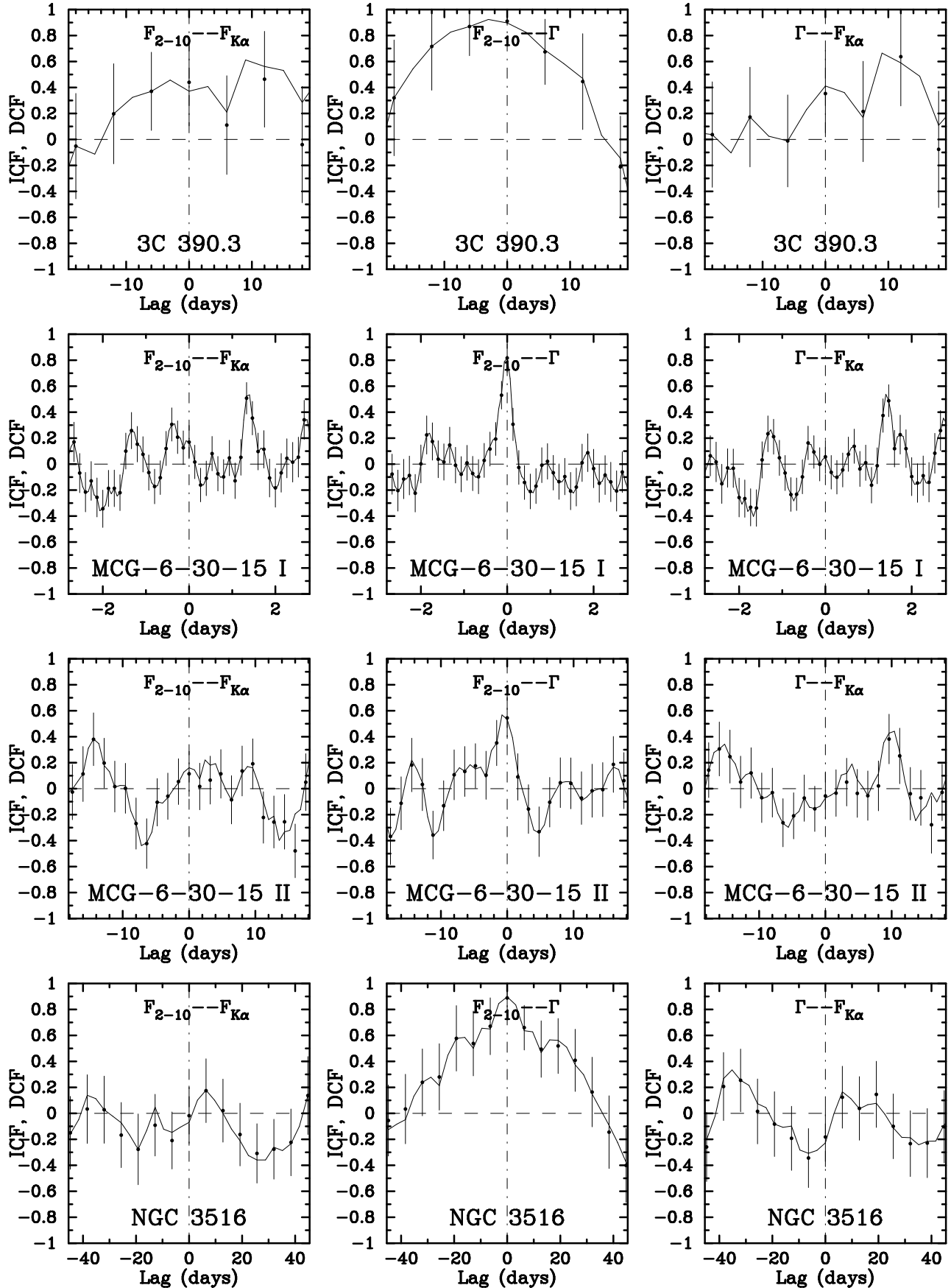


FIG. 3.— Cross-correlation functions for the short time scale light curves. Lags are defined such that a positive lag means the first light curve leads the second.

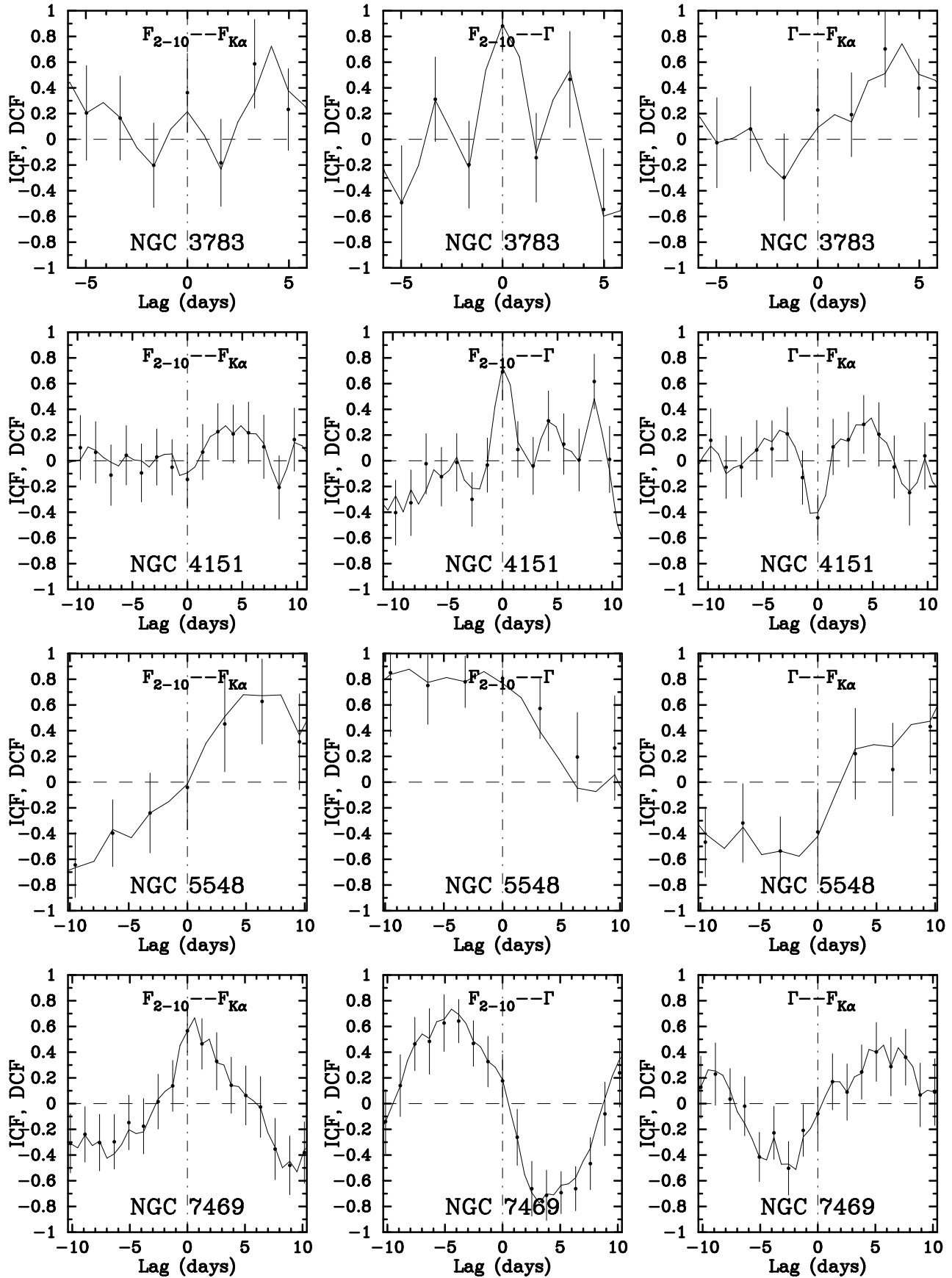


FIG. 3.— Figure 3, cont'd

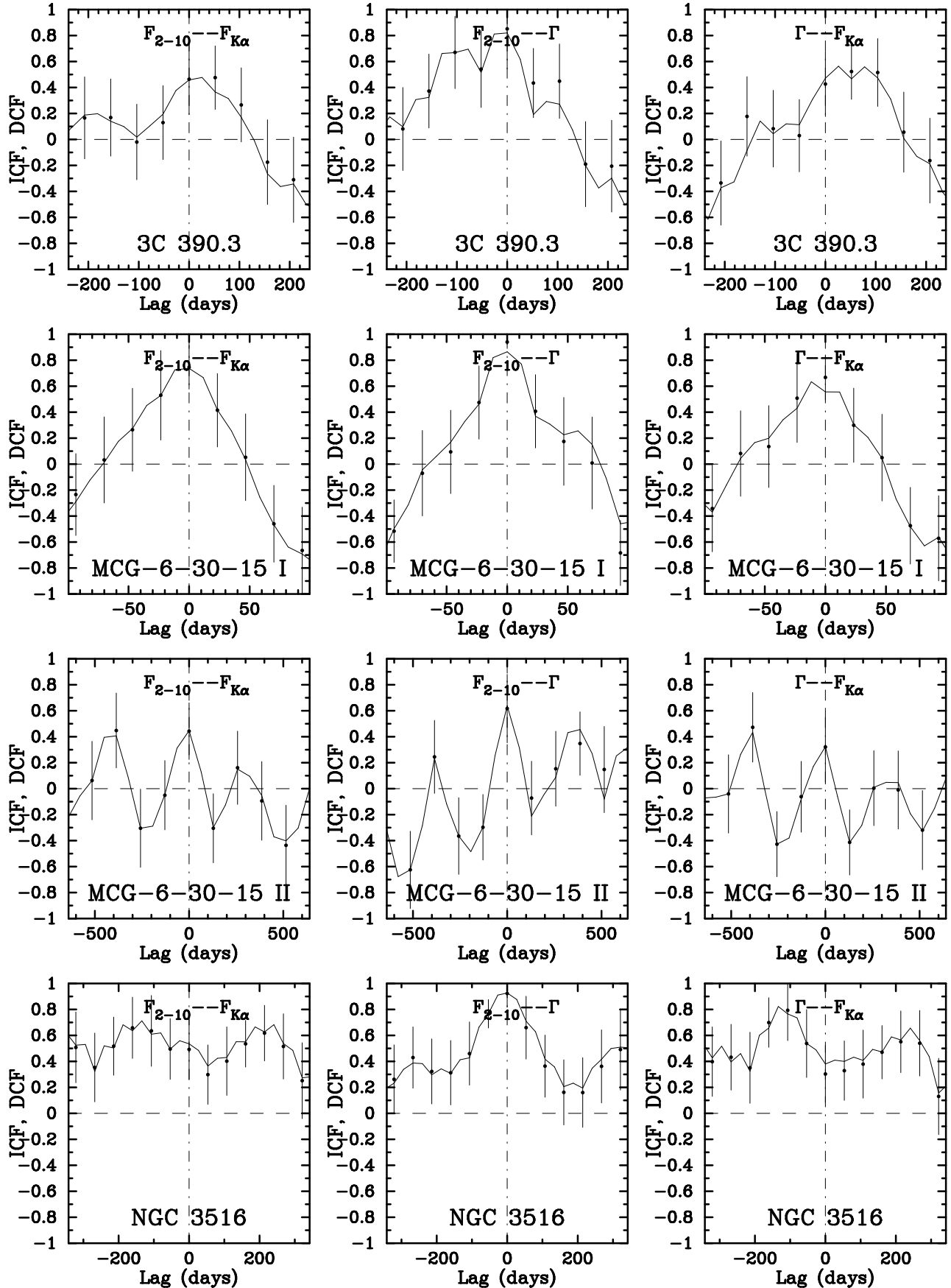


FIG. 4.— Cross-correlation functions for the long time scale light curves. Lags are defined such that a positive lag means the first light curve leads the second.

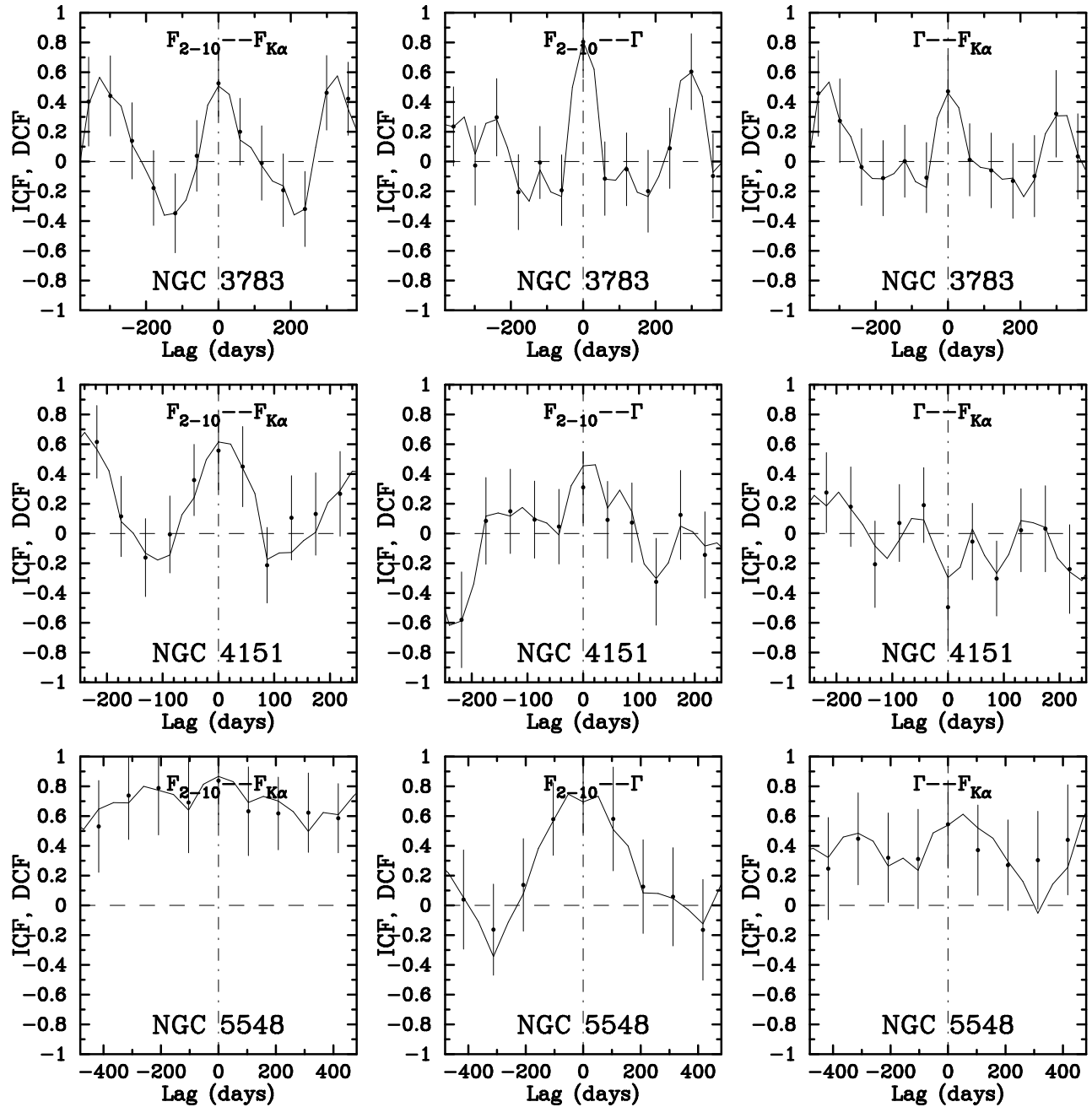


FIG. 4.— Figure 4, cont'd

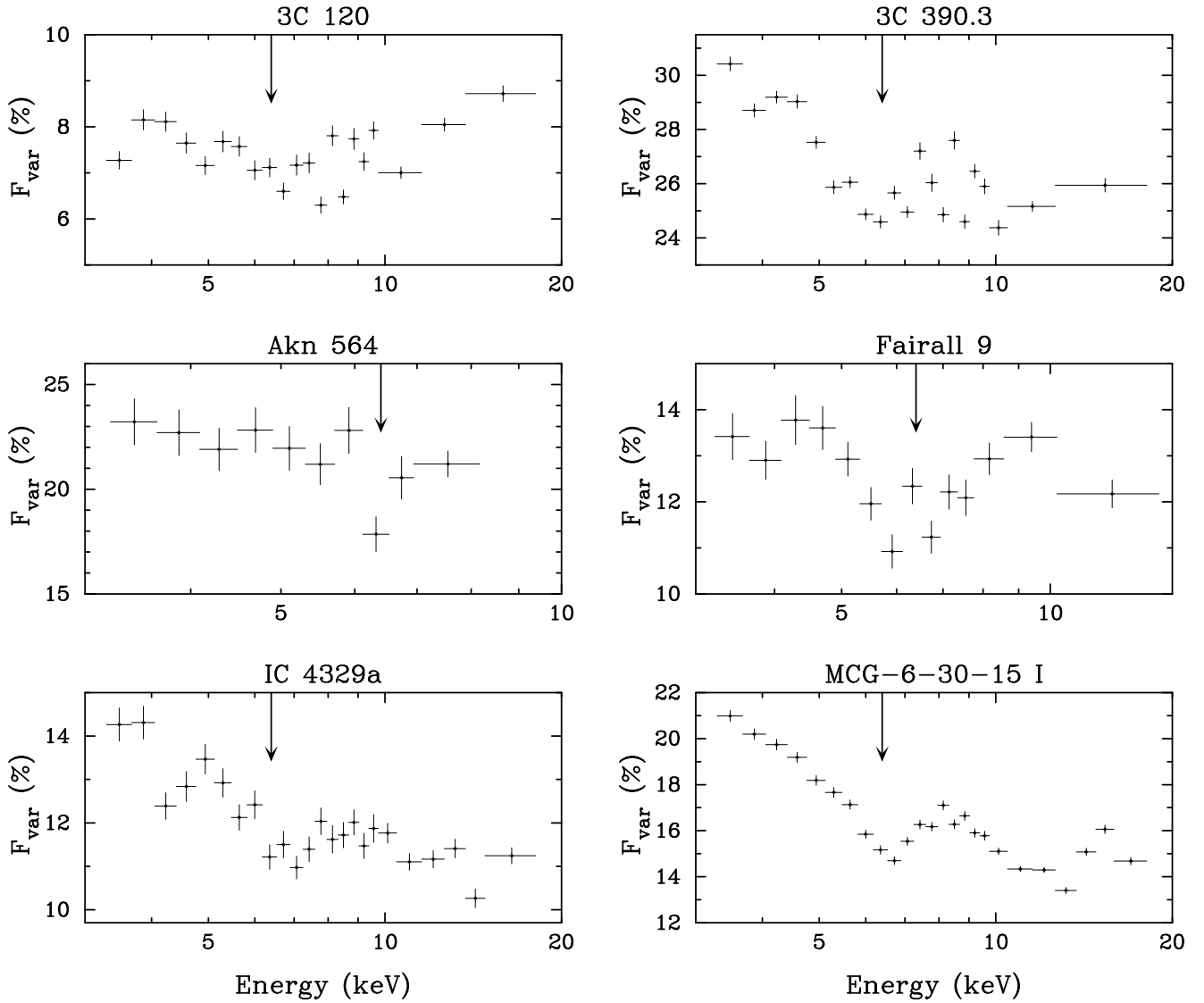


FIG. 5.— Short time scale F_{var} spectra. The downward arrows at 6.4 keV indicate the depression in broadband continuum variability due to relatively reduced Fe K_{α} line variability.

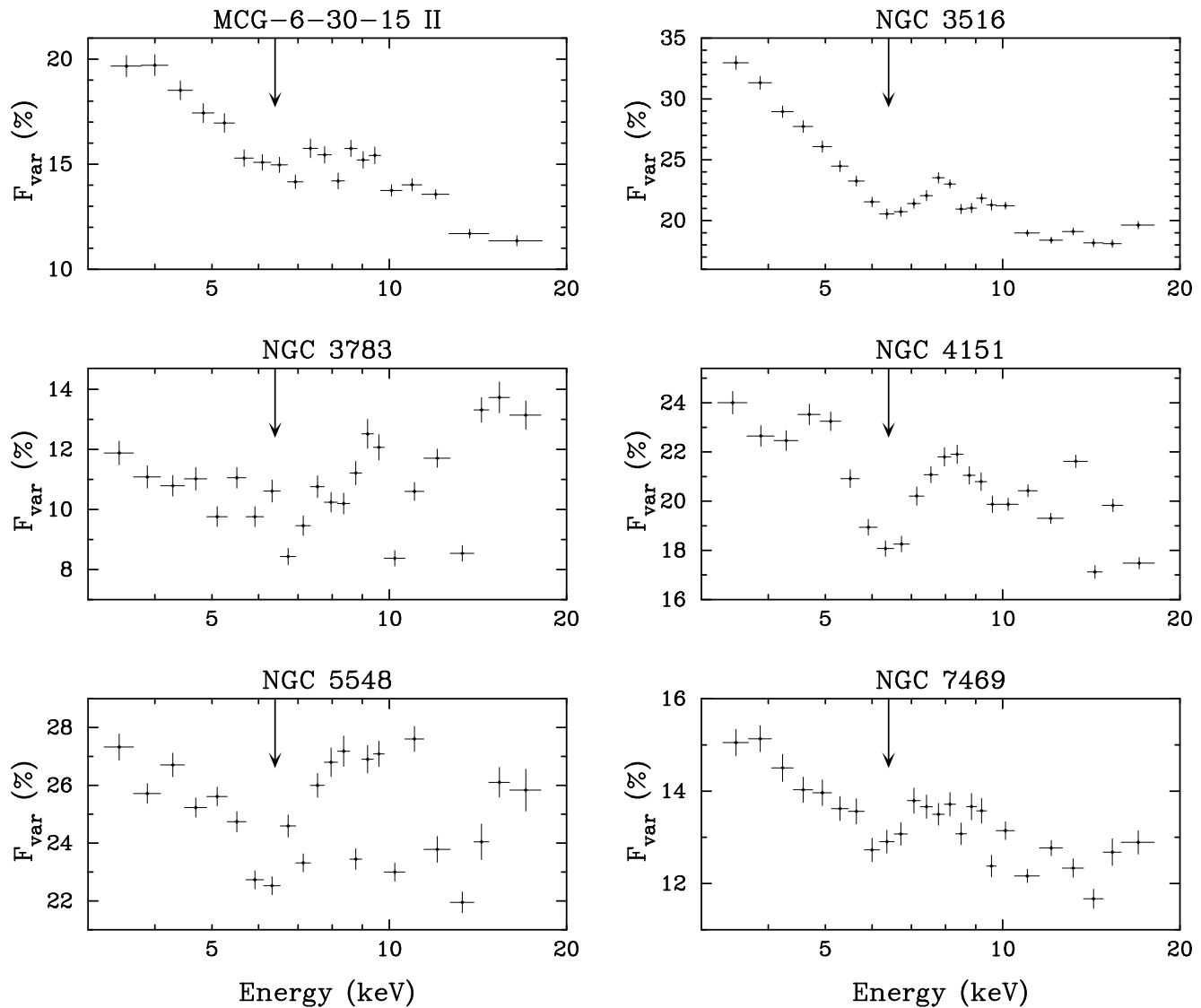


FIG. 5.— Figure 5, cont'd

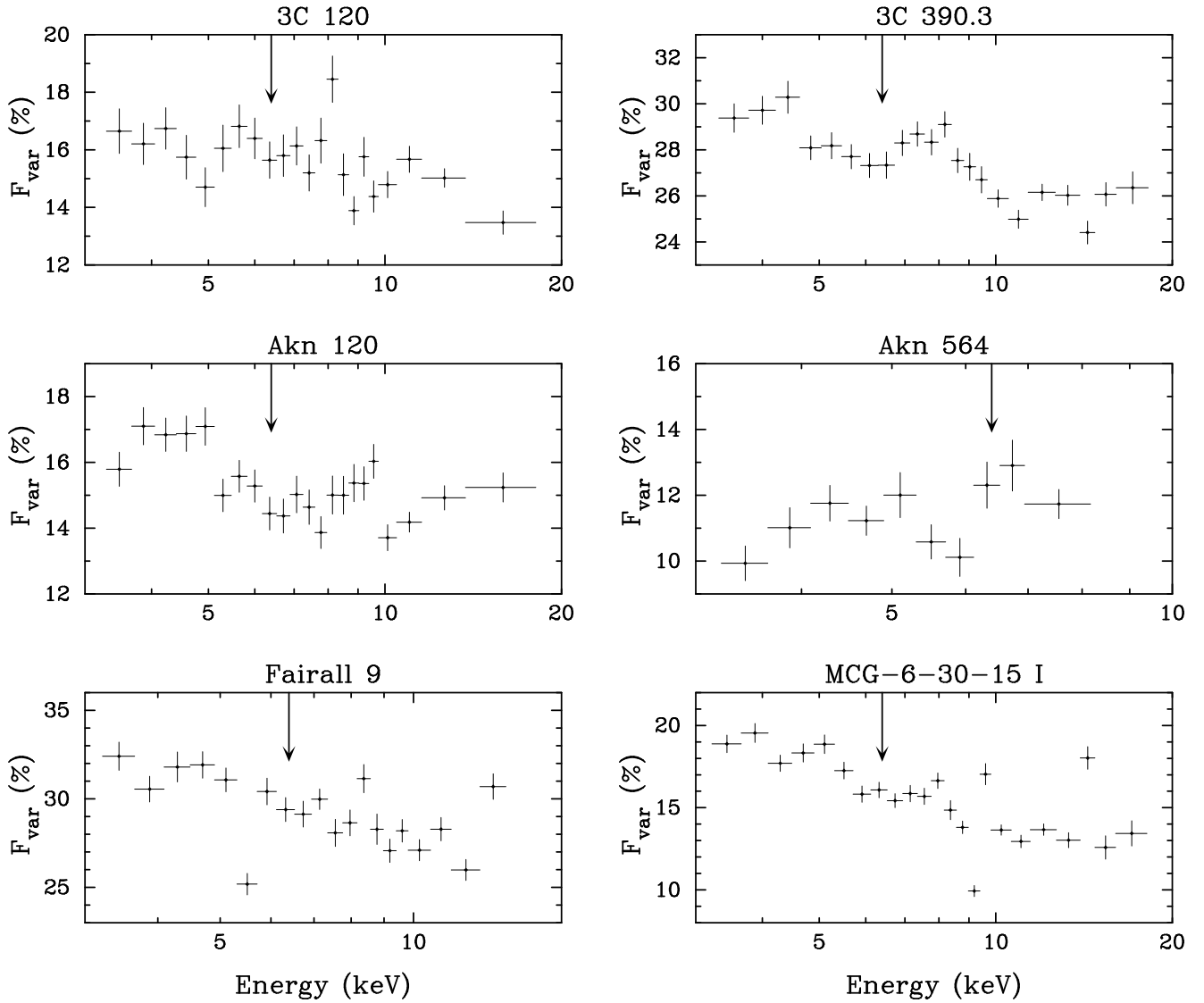


FIG. 6.— Long time scale F_{var} spectra. The downward arrows at 6.4 keV indicate the depression in broadband continuum variability due to relatively reduced Fe K_{α} line variability.

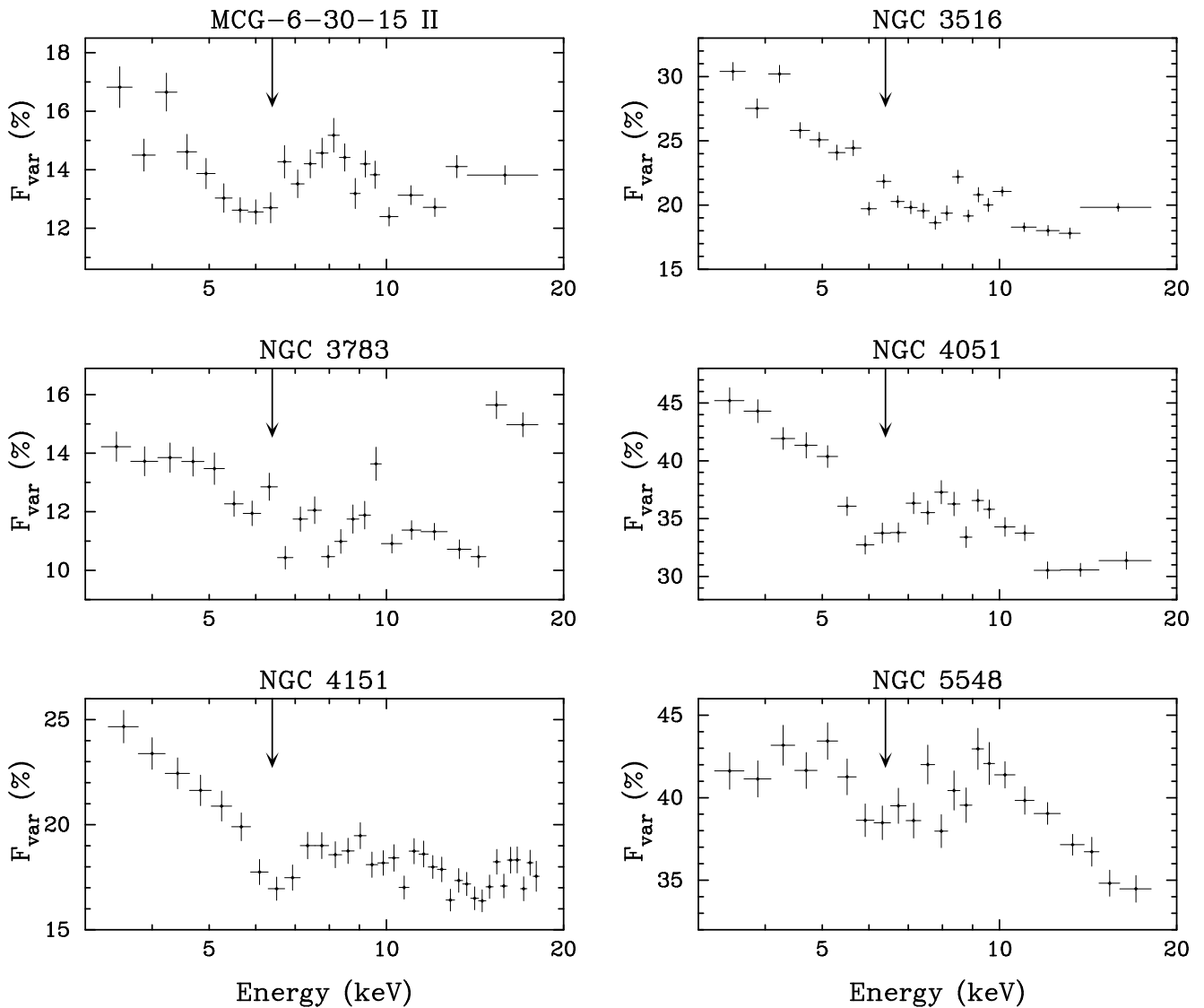


FIG. 6.— Figure 6, cont'd